



Gravitational collapse of rotating supermassive stars including nuclear burning effects

Haruki Uchida,¹ Masaru Shibata,² Takashi Yoshida,³ Yuichiro Sekiguchi,⁴ and Hideyuki Umeda³

¹*Yukawa Institute for Theoretical Physics, Kyoto University, Kyoto 606-8502, Japan*

²*Center for Gravitational Physics, Yukawa Institute for Theoretical Physics, Kyoto University, Kyoto 606-8502, Japan*

³*Department of Astronomy, Graduate School of Science, the University of Tokyo, Tokyo 113-0033, Japan*

⁴*Department of Physics, Toho University, Funabashi, Chiba 274-8510, Japan*

(Received 30 March 2017; published 24 October 2017)

Supermassive stars (SMSs) of mass $\gtrsim 10^5 M_\odot$ are candidates for seeds of supermassive black holes found in the center of many massive galaxies. We simulate the gravitational collapse of a rigidly rotating SMS core including nuclear burning effects in axisymmetric numerical relativity. We consider SMS cores composed of primordial metallicity and of helium in this paper. We find that for our chosen initial conditions, the nuclear burning does not play an important role. After the collapse, a torus surrounding a rotating black hole is formed and a fraction of the torus material is ejected by a hydrodynamical effect. We quantitatively study the relation between the properties of these objects and rotation. We find that if a SMS core is sufficiently rapidly rotating, the rest mass of the torus and outflow are approximately 6% and 1% of the initial rest mass, respectively. The typical average velocity and the total kinetic energy of the outflow are $0.2c$ and 10^{54-56} erg where c is the speed of light. Finally, we briefly discuss the possibility for observing the outflow, ringdown gravitational waves associated with the formation of black holes, and gravitational waves from the torus.

DOI: [10.1103/PhysRevD.96.083016](https://doi.org/10.1103/PhysRevD.96.083016)

I. INTRODUCTION

Recent observations have discovered strong evidence that many galaxies harbor a supermassive black hole (SMBH) in their center. However, the formation process of SMBHs still remains unsolved. One possible scenario is the so-called direct-collapse scenario [1]. In this scenario, one supposes that a supermassive star (SMS) with mass $\gtrsim 10^5 M_\odot$ is formed in a very hot primordial gas cloud with its virial temperature $\gtrsim 10^4$ K, and it subsequently forms a high-mass seed black hole through gravitational collapse. Recently, a luminous metal-free galaxy is detected at $z = 6.6$ and it is suspected to have a direct collapse black hole [2,3]. We note that for such high-temperature environment, a mass-accretion rate to the growing SMS with $> 0.1 M_\odot/\text{yrs}$ is possible [4].

During the gas accretion, the temporal mass accretion rate, \dot{M}_{BH} , is naively bounded by the Eddington rate such that

$$\dot{M}_{\text{BH}} = \frac{1 - \xi}{\xi} \frac{4\pi G m_p}{c \sigma_T} M_{\text{BH}}, \quad (1.1)$$

where G , c , ξ , m_p , σ_T , and M_{BH} are the gravitational constant, the speed of light, the energy conversion rate by accretion (< 1), the mass of proton, the Thomson scattering cross section, and the temporal mass of the black hole, respectively. Then we can estimate the growth time by solving Eq. (1.1) and get

$$t_{\text{growth}} \approx 0.12 \times \log_{10} \left(\frac{M_{\text{BH}}}{M_{\text{seed}}} \right) \text{Gyr}, \quad (1.2)$$

where M_{seed} is the mass of the seed black hole and we take $\xi = 0.1$. For a SMBH with mass $10^7 M_\odot$, which is the typical mass of SMBHs in local spiral galaxies [5], and for $M_{\text{seed}} = 100 M_\odot$, which is a typical value of first stars [6], we get $t_{\text{growth}} = 0.58$ Gyr. On the other hand, in the direct-collapse scenario, inserting $M_{\text{seed}} = 10^5 M_\odot$ and $M_{\text{BH}} = 10^7 M_\odot$ to Eq. (1.2), we get $t_{\text{growth}} = 0.23$ Gyr. Thus the condition for the mass accretion rate to form SMBHs is relaxed. This scenario is also thought to be one possible scenario that could form SMBHs in the early universe at redshift $z > 6$ (e.g., Refs. [7,8]). We note that there is another possible scenario that supercritical accretion (the mass accretion which rate is larger than the Eddington rate) could help the stellar mass BHs to grow up rapidly to the SMBHs [9–11].

Recent researches for SMS formation in spherical symmetry (e.g., Refs. [12–15]) have proposed that a SMS with mass $\gtrsim 2 \times 10^5 M_\odot$ could be formed if the mass-accretion rate reaches $0.1 M_\odot/\text{yrs}$ (i.e., the temperature of a primordial gas cloud becomes $\gtrsim 10^4$ K) and lasts for more than the period of nuclear-burning phases ($\approx 2 \times 10^6$ yrs [16]). To achieve such high virial temperature, there should not exist molecular hydrogen (H_2) in a primordial gas cloud. In the absence of H_2 , the gas cloud could reach this virial

temperature because atomic hydrogen cooling could achieve only about 10^4 K [17]. There are several routes to destroy H_2 molecules such as photodissociation by Lyman-Werner radiation from nearby local star formation regions [17–19] or collisional dissociation in the cold accretion flows in the forming first galaxies [20].

Latest numerical simulations suggest that SMSs are rotating because the environments surrounding each protostar of SMSs are not spherically symmetric (e.g., Refs. [21–24]). Also SMS cores seem to be rigidly rotating because convection is strongly enhanced if they are in nuclear-burning phases [13,16,21].

If SMSs have sufficiently large mass, they may collapse due to the so-called general-relativistic radial instability (e.g., Ref. [25]). If a SMS core is rotating, the condition for a SMS core to become unstable to the gravitational collapse is greatly different from the nonrotation case because rotation strongly stabilizes a SMS core (e.g., Refs. [26–30]). Our previous result suggests that SMS cores can be stable unless their mass exceeds about $6.3 \times 10^5 M_\odot$ in the hydrogen-burning phase and $2.3 \times 10^5 M_\odot$ in the helium-burning phase if they are rotating at mass-shedding limit [30]. These critical values are about 5 times larger than those for nonrotating SMSs.

SMSs have not been directly observed yet. However, in its presence, the gravitational collapse of SMS cores could be observed. Our previous study [31] proposed that if a SMS core is rotating, gravitational waves associated with the quasi-normal mode ringdown are emitted during the black-hole formation and if it occurs at the cosmological redshift less than ≈ 3 , the signal will be detectable by space laser interferometric detectors like Laser Interferometer Space Antenna (LISA) [32]. If a supermassive star is rapidly and extremely differentially rotating, it would form two supermassive black holes during the collapse, and their inspiral and merger emit strong gravitational waves which are detectable at redshift $z \gtrsim 10$ by the DECIGO or the Big Bang Observer [33]. Other studies show that a collapsing SMS may be detectable as a gamma-ray burst or an ultraluminous supernova if the formed black hole launches a relativistic jet during the collapse [34,35].

The primary purpose of this paper is to explore the effects of nuclear burning in the collapse of SMSs and for the remnants of the SMS collapse. For the effect of nuclear burning, there are several pioneering studies that indicate that its effect may change the SMS collapse into an explosion like pair instability supernovae [36–38]. However, they focused only on a restricted class of the gravitational collapse of SMS cores. In Refs. [36,37], the authors considered SMS cores of primordial composition as well as varying initial metallicities (just the abundance of CNO) with the inclusion of nuclear reactions and discovered that a SMS core would explode by the ignition of the hydrogen during the collapse phase if its initial metallicity is larger than $O(10^{-3})$. In Ref. [38], they considered

nonrotating SMSs and concluded that a SMS with mass close to $\approx 55500 M_\odot$ would explode due to helium burning. In reality, the typical metallicity of the SMS core at hydrogen burning phase will be $O(10^{-9})$ because a supermassive protostar’s initial contraction will continue until triple-alpha reaction produces such a small fraction of CNO for hydrogen-burning through the CNO cycle by which the protostar will reach a hydrostatic equilibrium [16]. It is also natural to consider that SMSs would be rapidly rotating [24]. Moreover, no study has paid special attention to the evolution of the remnant formed after the SMS core collapse.

In this paper, we perform general-relativistic simulations of the gravitational collapse of rotating SMS cores from plausibly realistic initial conditions including the effects of nuclear burning and rotation. We will show that for the initial conditions we employ, a black hole is formed irrespective of the presence of the nuclear burning effect. In addition, a torus surrounding the black hole is formed. We will also show that for the evolution of the torus, the nuclear burning effect does not play an important role.

After the black-hole formation, a fraction of the torus material is ejected as an outflow due to purely hydrodynamical effect. We will describe the formation process of the outflow (see Ref. [39] as a pioneering study). We will show that if the initial SMS core is sufficiently rapidly rotating, the typical total kinetic energy and speed of the outflow are 10^{54-56} erg and $0.2c$, respectively.

The paper is organized as follows. In Sec. II, we describe the setup of our numerical simulation. In Sec. III, we describe the overview of the collapse showing our results of numerical simulations and discuss the effects of nuclear burning. We also study the dependence of the mass of the torus surrounding a black hole formed after the collapse on the rotation and adiabatic constant. In Sec. IV, we describe the formation process of the outflow and explore its properties. In Sec. V, we discuss the possibility for observing the outflow and gravitational waves. Section VI is devoted to the conclusion.

II. NUMERICAL SETUP

A. Calculation of gravitational field

For solving Einstein’s evolution equations, we use the same method as in Ref. [31]. We employ the original version of BSSN (Baumgarte-Shapiro-Shibata-Nakamura) formalism with a puncture gauge [40–43]. In the $3+1$ formulation, the metric is defined by the form

$$ds^2 = -\alpha^2 c^2 dt^2 + \gamma_{ij}(dx^i + \beta^i c dt)(dx^j + \beta^j c dt), \quad (2.1)$$

where α , β^i , and γ_{ij} are the lapse function, the shift vector, and the induced metric on three-dimensional (3D) spatial hypersurfaces, respectively. We also define the extrinsic curvature by

$$K_{ij} \equiv -\gamma_i^\alpha \gamma_j^\beta \nabla_\alpha n_\beta, \quad (2.2)$$

where n^μ is a timelike unit-normal vector orthogonal to three-dimensional (3D) hypersurfaces. In the BSSN formalism, we evolve $\rho_g \equiv (\det \gamma_{ij})^{-1/6}$, $\tilde{\gamma}_{ij} \equiv \rho_g^2 \gamma_{ij}$, $\tilde{A}_{ij} \equiv \rho_g^2 (K_{ij} - \gamma_{ij} K_k^k / 3)$, K_k^k , and $F_i \equiv \delta^{jk} \partial_j \tilde{\gamma}_{ik}$. We use the standard 4th-order finite differencing scheme to solve the gravitational-field equations (see chapter 3 of [44] for a review).

A previous work indicates that if a SMS core is rigidly rotating, there would be essentially no nonaxisymmetric deformation during the collapse [45]. Hence we assume the axial symmetry and use a 4th-order cartoon method to impose this condition to the gravitational field [46,47]. We neglect viscosity because the time scale of the gravitational collapse is much shorter than the viscous time scale. We only consider the collapse of SMS cores because the density of their envelope is very low, and hence, they are unlikely to affect the collapse dynamics and subsequent formation process of a black hole surrounded by a dense torus formed in the vicinity of the central region.

We perform numerical simulations in cylindrical coordinates (X, Z) , and a nonuniform grid is used for X and Z in the following manner. We define the grid spacing at the center by $\Delta X_0 \equiv X_1 - X_0$. Here $X_0 = 0$ and X_i is the location of i th grid. We use different manners of grid spacing inside and outside a grid X_{in} . For $X_i < X_{in}$, $\Delta X_i \equiv X_i - X_{i-1} = \Delta X_0 (\text{const})$, and for $X \geq X_{in}$, $\Delta X_i = \eta \Delta X_{i-1}$, where η is a constant. η determines the nonuniform degree of the grid spacing. We set $X_{in} \sim R_M$ where R_M is the gravitational radius defined by

$$R_M \equiv \frac{GM_0}{c^2}, \quad (2.3)$$

and M_0 is the initial gravitational mass of the SMS core.

We set outer boundaries of the computational domain at $\approx 600R_M$ along each axis. To calculate the propagation of the outflow, we expand the computational domain to $\approx 4800R_M$ along each axis after the formation of the central black hole. We set $\Delta X_0 \approx 0.037R_M$, $\eta = 1.018$ for the low-resolution case, $\Delta X_0 \approx 0.027R_M$, $\eta = 1.017$ for the middle-resolution case, and $\Delta X_0 \approx 0.023R_M$, $\eta = 1.014$ for the high-resolution case. We show that the numerical results have a good convergence property for our models in Sec. III.

B. Equations of the fluid

To self-consistently calculate the effect of nuclear burning, we follow the method employed in Ref. [48]. We introduce two categories of density, i.e., the rest-mass density, ρ_0 , and the baryon density, ρ , defined respectively by

$$\rho_0 = \sum_i m_i n_i (i = p, \alpha, C, e), \quad (2.4)$$

$$\rho = m_u (n_p + 4n_\alpha + 12n_C) = m_u n_B, \quad (2.5)$$

where m_u and n_B are the atomic mass unit and the baryon number density. We use m_i and n_i for the rest mass and number density of the i th species. Subscripts p, α , C, and e denote H, ^4He , ^{12}C , and electron, respectively. We also define the density of each nucleus by

$$\rho_i \equiv m_u A_i n_i (i = p, \alpha, C), \quad (2.6)$$

where A_i is the mass number for each nucleus. According to the electrical charge neutrality, n_e can be written as

$$n_e = n_p + 2n_\alpha + 6n_C. \quad (2.7)$$

Note that ρ is proportional to the baryon number density, and thus, it does not change by nuclear burning. Hence it is convenient to define thermodynamic quantities in terms of ρ .

We assume a perfect fluid, and thus, the energy momentum tensor is written as

$$T_{\mu\nu} = \rho h u_\mu u_\nu + P g_{\mu\nu}, \quad (2.8)$$

where

$$h \equiv \frac{\rho_0}{\rho} c^2 + \epsilon + \frac{P}{\rho}, \quad (2.9)$$

and ϵ , h , P , and u_μ are the internal energy per baryon, the enthalpy per baryon, pressure, and four velocity, respectively. We should be careful that ϵ and h are not equivalent to the specific internal energy and specific enthalpy, respectively. For evolving the four velocity and energy density, we solve the conservation equations for the energy momentum tensor,

$$\nabla_\mu T^{\mu\nu} = 0. \quad (2.10)$$

We note that we do not add any term in the right-hand side of Eq. (2.10).

In addition, we have to evolve ρ_i (not $\nabla_\mu (\rho u^\mu) = 0$) by solving the continuity equations. Before describing the equations for them, we shall mention the reason that we introduce ρ and ρ_0 independently. The difference between ρ and ρ_0 is defined by

$$\delta \equiv \frac{\rho_0}{\rho} - 1 = \Delta_p Y_p + \Delta_\alpha Y_\alpha + \Delta_C Y_C, \quad (2.11)$$

where

$$\Delta_p = \frac{1}{m_u} (m_p + m_e - m_u), \quad (2.12)$$

$$\Delta_\alpha = \frac{4}{m_u} \left(\frac{m_\alpha}{4} + \frac{m_e}{2} - m_u \right), \quad (2.13)$$

$$\Delta_C = \frac{12}{m_u} \left(\frac{m_C}{12} + \frac{m_e}{2} - m_u \right), \quad (2.14)$$

and $Y_i \equiv n_i/n_B = \rho_i/(\rho A_i)$.

Now, we demonstrate how the rest-mass energy is converted to the internal energy via nuclear burning. For simplicity, we shall use the fluid rest frame in the following analysis. Then, the rest-mass energy density released via the nuclear burning can be written as

$$dE = -d\rho_0 c^2, \quad (2.15)$$

where d denotes the difference between before and after the nuclear burning. Using Eq. (2.11) and $d\rho = m_u dn_B = 0$, Eq. (2.15) can be rewritten as

$$dE = -\rho c^2 d\delta. \quad (2.16)$$

This equation denotes that the released rest-mass energy is proportional to the variation of δ . The total energy density should be conserved, and hence,

$$d(\rho_0 c^2 + \rho \epsilon) = 0. \quad (2.17)$$

Inserting Eqs. (2.15) and (2.16) to Eq. (2.17), we get

$$d(\rho \epsilon) = dE = -\rho c^2 d\delta. \quad (2.18)$$

Therefore the released rest-mass energy is autonomically converted to the increase of the internal energy via the decrease of δ . Actually, some fraction of the released rest-mass energy is emitted by neutrinos, and thus, this formalism slightly overestimates the increase of the internal energy.

If we consider the effect of nuclear burning, the continuity equations for each nucleus should be written as

$$\nabla_\mu(\rho_i u^\mu) = S_i (i = p, \alpha, C), \quad (2.19)$$

where S_i is the source term due to the nuclear burning for each nucleus. The baryon number density should be conserved (i.e., $\nabla_\mu(\rho u^\mu) = 0$), and hence, S_i should satisfy the equation

$$S_p + S_\alpha + S_C = 0. \quad (2.20)$$

Our method for numerically solving Eq. (2.19) will be described in Sec. II D.

C. Equation of state

We assume that the equation of state (EOS) during the collapse can be written as a sum of the ideal gas and radiation, i.e.,

$$P = \frac{1}{3} a T^4 + \frac{Y_T k_B}{m_u} \rho T, \quad (2.21)$$

$$\epsilon = \frac{a T^4}{\rho} + \frac{3 Y_T k_B}{2 m_u} T, \quad (2.22)$$

where a , k_B , and T are the radiation constant, Boltzmann constant, and temperature, respectively. Y_T is defined by

$$Y_T = Y_p + Y_\alpha + Y_C + Y_e. \quad (2.23)$$

We write the mass fraction of each nucleus as $X_\alpha = 4Y_\alpha$ and $Z_C = 12Y_C$. If a SMS core is in the ZAMS phase, their typical values are approximately $(Y_p, X_\alpha, Z_C) \approx (0.75, 0.25, 0)$, leading to $Y_T \approx 1.69$ and if a SMS core is just at the onset of the helium burning phase, $(Y_p, X_\alpha, Z_C) \approx (0, 1, 0)$, and thus, $Y_T \approx 0.75$.

This EOS is valid unless electrons become relativistic, degenerate, or the effects of pair creation of electron-positron pairs cannot be neglected. That is, this approximation is valid within the range of $\rho < 10^6$ g/cm³ and $T < 10^9$ K. Actually, just before black hole is formed, the central region of the collapsing SMS core would be out of this range but our simulations show that this region immediately falls into the black hole. Hence it will be safe to consider that the EOS composed of Eqs. (2.21) and (2.22) is appropriate for our present study.

D. Nuclear burning

By using the baryon number conservation equation (i.e., $\nabla_\mu(\rho u^\mu) = 0$), Eq. (2.19) can be rewritten as

$$\frac{\partial Y_i}{\partial t} + v^j \frac{\partial Y_i}{\partial x^j} = \frac{S_i}{\rho u^t}, \quad (2.24)$$

where $v^j = u^j/u^t$. It is not an easy task to simultaneously solve the advection and the nuclear burning network. Thus we divide Eq. (2.24) into two parts (i.e., operator splitting approach is employed). First, we solve the advection equations without nuclear burning, that is,

$$\frac{\partial Y_i}{\partial t} + v^j \frac{\partial Y_i}{\partial x^j} = 0. \quad (2.25)$$

This is equivalent to solving

$$\nabla_\mu(\rho_i u^\mu) = 0 (i = p, \alpha, C). \quad (2.26)$$

Second, we solve equations of nuclear burning reactions such as

$$\frac{\partial Y_p}{\partial t} = \frac{S_p}{\rho u^t} = \frac{m_u}{u^t} \left(-\frac{\dot{q}_{\text{CNO}}}{Q_{\text{CNO}}} \right), \quad (2.27)$$

$$\frac{\partial Y_\alpha}{\partial t} = \frac{S_\alpha}{\rho u^t} = \frac{m_u}{4u^t} \left(\frac{\dot{q}_{\text{CNO}}}{Q_{\text{CNO}}} - \frac{\dot{q}_{3\alpha}}{Q_{3\alpha}} \right), \quad (2.28)$$

$$\frac{\partial Y_C}{\partial t} = \frac{S_C}{\rho u^t} = \frac{m_u}{12u^t} \left(\frac{\dot{q}_{3\alpha}}{Q_{3\alpha}} \right), \quad (2.29)$$

where \dot{q}_J and Q_J ($J = \text{CNO}, 3\alpha$) are the energy generation rate and the energy liberated per baryon of CNO cycle and triple-alpha reaction, respectively. \dot{q}_J has units of erg/g/s. In this paper, we only consider cold CNO cycle, hot CNO cycle, and triple-alpha reactions. For \dot{q}_J , we employ the same formulas as those of Ref. [37] [see Eqs. (25)–(27) for this reference]. We also simulated the gravitational collapse including the effect of the rp-process using the same formalism as Ref. [37] as test calculations and found that the rp-process affects only weakly the gravitational collapse for models A1 and A3 (see Sec. III A) because this process becomes efficient only in the very dense and hot region. The previous studies also show that the rp-process is inefficient for the gravitational collapse of SMSs [36,37]. Thus, for the product runs, we neglect the rp-process.

We find that when we employ an initial condition with large metallicity ($Z_{\text{CNO}} \gtrsim 10^{-3}$), the results of simulations between our formalism and the formalism employed in Ref. [37] do not agree with each other. We briefly illustrate the validity of our calculation of nuclear burning in Appendix A.

We also compute the neutrino generation rate using the formulation of Ref. [49] [see Eqs. (2.1), (3.2), and (4.1) for this reference], but we do not include the effect of neutrino cooling in our simulations because it is much weaker than the effect of nuclear burning outside the formed black hole except just before the black-hole formation (see Sec. III B). At the black-hole formation, the neutrino cooling rate would become larger than the nuclear burning heating rate. However at this time, most of the generated neutrinos would be absorbed by the black hole. Thus, we assume that the neutrino cooling would be negligible throughout the collapse.

E. Initial conditions

Following our previous paper [30], we first prepare equilibrium states of SMS cores which are marginally stable to the general-relativistic quasiradial instability. We briefly review the method as follows.

In the stationary and axisymmetric spacetime, the spacetime line element can be written by

$$ds^2 = -e^{\gamma_s + \rho_s} c^2 dt^2 + e^{2\alpha_s} (dr^2 + r^2 d\theta^2) + e^{\gamma_s - \rho_s} r^2 \sin^2 \theta (d\varphi - \omega_s dt)^2, \quad (2.30)$$

where $\rho_s, \gamma_s, \alpha_s$, and ω_s are functions of r and θ .

The EOS employed is the same as Eqs. (2.21) and (2.22). Using the first law of thermodynamics, the adiabatic constant Γ is calculated as [16]

$$\Gamma = \left(\frac{\partial \ln P}{\partial \ln n_B} \right)_s = \frac{4}{3} + \frac{4\sigma + 1}{3(\sigma + 1)(8\sigma + 1)}, \quad (2.31)$$

where σ is the ratio of the radiation pressure to the gas pressure defined by

$$\sigma \equiv \frac{aT^3}{3Y_T n_B k_B} = \frac{s_\gamma}{4Y_T k_B}. \quad (2.32)$$

Here s_γ and $s = s_\gamma + s_g$ are the photon entropy per baryon and the total (photon and gas) entropy per baryon, respectively. If SMS cores are in nuclear-burning phases, they should be fully convective (e.g., Refs. [13,16]). Hence, it is natural to assume that SMS cores are isentropic ($s = \text{constant}$), its chemical composition is uniform ($Y_I = \text{constant}$), and they are rigidly rotating. Furthermore in SMS cores, $s_\gamma \gg s_g$ are realized [16,50] so that s_γ is also nearly constant. Then σ can be assumed to be constant. As a result, Eq. (2.31) can be easily integrated by n_B , and we get the polytropics EOS

$$P = K \rho_0^\Gamma, \quad \Gamma = 1 + \frac{1}{N}, \quad (2.33)$$

where K and N are the polytropic constant and the polytropic index, respectively. K is written as

$$K \approx \left(\frac{Y_T k_B \sigma}{m_u} \right)^{\frac{4}{3}} \left(\frac{3}{a} \right)^{\frac{1}{3}} (1 + \sigma^{-1}) \rho_0^{-1/(6\sigma)}. \quad (2.34)$$

Here, the density dependence of K can be neglected because $\sigma \gg 1$ for typical SMS cores. We use this polytropic EOS in computing equilibrium states and assume that the energy momentum tensor has the same form as Eq. (2.8).

For SMS cores, their density profile is approximately described by the Lane-Emden solution of $N = 3$ even if they are rotating at mass-shedding limit (e.g., Ref. [51]). Then by using this solution, the mass of the SMS core, M , can be approximately written as

$$M \approx 4.555 G^{-\frac{2}{3}} K^{\frac{3}{2}}. \quad (2.35)$$

(This is equivalent to approximating $C_{n_p} = C_3$ of Ref. [30].)

Using Eqs. (2.31), (2.33), (2.34), and (2.35), Γ can be approximately rewritten as

$$\Gamma - \frac{4}{3} \approx \frac{1}{6\sigma} \approx 3.8 \times 10^{-3} \left(\frac{M}{10^5 M_\odot} \right)^{-\frac{1}{2}} \left(\frac{Y_T}{1.69} \right), \quad (2.36)$$

where we used $\sigma \gg 1$. Inserting Eqs. (2.32)–(2.36), the relation among the central density, the central temperature, and the mass of the SMS core can be approximately written as

$$\frac{P_c}{\rho_{0c} c^2} \sim 1.1 \times 10^{-3} \left(\frac{T_c}{10^{8.2} \text{K}} \right) \left(\frac{M}{10^5 M_\odot} \right)^{\frac{1}{2}}, \quad (2.37)$$

where the index c denotes the central value of the SMS core.

We define two dimensionless parameters, y and β , by

$$y \equiv 2.6324 \frac{P_c}{\rho_{0c} c^2}, \quad (2.38)$$

and

$$\beta \equiv \frac{T_{\text{rot}}}{|W|}. \quad (2.39)$$

Here T_{rot} and W denote the rotational kinetic energy and the gravitational potential energy defined by

$$T_{\text{rot}} \equiv \frac{1}{2} J_K \Omega, \quad (2.40)$$

$$W \equiv M_K c^2 - M_p c^2 - T_{\text{rot}}, \quad (2.41)$$

where Ω , J_K , M_K , and M_p are the angular velocity, Komar angular momentum, Komar mass (gravitational mass), and the proper mass defined by

$$J_K \equiv 2\pi \int \rho_0 h u^t u_\phi e^{2\alpha_s + \gamma_s} r^2 dr d\cos\theta, \quad (2.42)$$

$$M_K \equiv \frac{2\pi}{c^2} \int (-2T'_t + T''_\mu) e^{2\alpha_s + \gamma_s} r^2 dr d\cos\theta, \quad (2.43)$$

and

$$M_p \equiv \frac{2\pi}{c} \int \rho_0 u^t (c^2 + \epsilon) e^{2\alpha_s + \gamma_s} r^2 dr d\cos\theta, \quad (2.44)$$

respectively.

According to our previous result [30], the condition for SMS cores to be marginally stable to gravitational collapse can be written as

$$\Gamma - \frac{4}{3} = y - y^2 - \left(\frac{10}{3} - 2\Gamma - y - \beta \right) \beta. \quad (2.45)$$

If the value of the left-hand side of Eq. (2.45) is smaller than the right-hand side, the SMS core is unstable. Using

Eqs. (2.36)–(2.45), the mass of the SMS core which is marginally stable can be approximately written as

$$M_5^{\frac{1}{2}} = \frac{\beta_{-3} + \sqrt{\beta_{-3}^2 + 99 T_{8.2} Y_{T1.69}}}{8.7 T_{8.2}}, \quad (2.46)$$

where

$$M_5 \equiv \left(\frac{M}{10^5 M_\odot} \right), \quad T_{8.2} \equiv \left(\frac{T_c}{10^{8.2} \text{K}} \right), \\ Y_{T1.69} \equiv \left(\frac{Y_T}{1.69} \right), \quad \beta_{-3} \equiv \left(\frac{\beta}{10^{-3}} \right). \quad (2.47)$$

If a SMS core is in nuclear burning phases, its surface luminosity, L , and its energy generation rate of nuclear burning, \dot{Q} should agree with each other. Here, L and \dot{Q} are defined by

$$L \equiv -\frac{4ac}{3\kappa} \int_S \frac{1}{\rho_0} \nabla^i (T^4) dS_i, \quad (2.48)$$

$$\dot{Q} \equiv \int_{V_S} \rho_0 \dot{q} dV, \quad (2.49)$$

where κ , S , and V_S denote the opacity, the surface and the volume of the SMS core, respectively. We assume that the opacity is dominated by Thomson scattering of free electrons, i.e., $\kappa = 0.4 Y_e \text{ cm}^2/\text{g}$.

We use an iteration method to derive the equilibrium state of marginally stable SMS cores using Eqs. (2.32), (2.45), (2.48), and (2.49) as follows. The input parameters are the chemical composition Y_I ($I = p, \alpha, C$) and the rotation parameter β .

- (1) Provide input parameters Y_I ($I = p, \alpha, C$) and β .
- (2) Provide a temporal value of y .
- (3) Calculate the adiabatic constant Γ by using Eq. (2.45). Then by using Eqs. (2.31), (2.32) and (2.34), we determine the polytropic constant K .
- (4) Numerically compute $\rho_s, \gamma_s, \alpha_s, \omega_s$, and the density profile of the SMS core by solving the set of equations for stationary axisymmetric rotating equilibrium in general relativity by using the method of Ref. [50].
- (5) Calculate the temperature profile from Eq. (2.32).
- (6) Calculate \dot{Q} and L . If $\dot{Q} > L$, we decrease y , and otherwise, we increase y , and return to step 3.

We iteratively perform the procedures 1–6 until $|\dot{Q} - L|$ becomes sufficiently small.

In numerical simulations, we initially reduce the temperature uniformly as the initial perturbation. We define a perturbation parameter D_T such that the perturbed temperature can be written as

$$T = \left(1 - \frac{D_T}{100}\right) T_0, \quad (2.50)$$

where T_0 is the unperturbed temperature. We perform simulations for $D_T = 0.5, 0.25, 0.125,$ and 0.0625 , respectively (this is approximately the same as uniformly reducing the pressure by 2%, 1%, 0.5%, and 0.25%, respectively).

After adding the perturbation, the configuration does not satisfy the constraint equations, and hence, we once more solve the constraint equations.

III. RESULT

A. Overview of the collapse

We performed numerical relativity simulations for four initial states of SMS cores listed in Table I. Basically, the simulations are performed for the middle grid resolution with $D_T = 0.5$. For selected models, the simulations are performed for different grid resolutions and for different values of D_T (see, e.g., Figs. 2 and 3). Models A1 and A3 are assumed to be in the ZAMS phase, and A2 and A4 are just at the onset of the helium-burning phase. For models A1 and A3, we set that the initial metallicity is of order 10^{-9} because a supermassive protostar will continue to contract until triple-alpha burning produces CNO of $Z_{\text{CNO}} \approx 10^{-9}$ for hydrogen-burning through the CNO cycle which allows the protostar to reach a hydrostatic equilibrium [16].

Figure 1 displays snapshots of the rest-mass density profiles for the collapse of a SMS core to a black hole and a torus surrounding it for model A4. The lower panels are the snapshots at the same time as the middle panels but they only depict unbound fluid elements. The black hole is formed at $t \approx 9400$ s (near the time of the 3rd panel). After the collapse, a torus surrounding the black hole is formed and a part of the mass becomes unbound and ejected. Qualitatively, the collapse dynamics for the other models is similar to model A4.

Figure 2 shows the evolution of the total mass outside the central black hole, $M_{\text{total}}(t)$, defined by

$$M_{\text{total}}(t) \equiv \int_{V'} \rho_{0*} dV, \quad (3.1)$$

TABLE I. Key quantities for SMS cores employed in this paper. $M_5 \equiv M_0/10^5 M_\odot$. ‘‘Shedd’’ means that the SMS core is at mass-shedding limit ($T_{\text{rot}}/|W| \approx 0.009$). Z_{C9} is defined by $Z_{\text{C}}/10^{-9}$. Γ is the initial polytropic index defined by Eq. (2.33). ρ_c and T_c are the initial central density and temperature, respectively.

Model	M_5	$T_{\text{rot}}/ W $	Y_p	X_α	Z_{C9}	Γ	phase	ρ_c [g/cm ³]	T_c [10 ⁸ K]
A1	1.99	0.002	0.75	0.25	5	1.3360	ZAMS	1.1	1.5
A2	0.47	0.002	0	1.0	0	1.3358	He-burning	17	3.0
A3	6.56	Shedd	0.75	0.25	5	1.3348	ZAMS	0.64	1.6
A4	1.57	Shedd	0	1.0	0	1.3347	He-burning	11	3.2

as a function of $t - t_{\text{BH}}$ where t_{BH} is the time of the black-hole formation. In Eq. (3.1), $V' \equiv V - V_{\text{BH}}$. V and V_{BH} are the 3D spatial volume of $t = \text{const}$ and the region inside the black hole, respectively. Before the black-hole formation, $V' = V$. $\rho_{0*} \equiv \rho_0 \sqrt{-g} c u^t$ and $dV \equiv 2\pi dX dZ$ are the weighted rest-mass density and the volume element, respectively. We note that t_{BH} for models A1, A2, A3, and A4 with $D_T = 0.5$ are 2.9×10^4 s, 7.3×10^3 s, 3.8×10^4 s, and 9.4×10^3 s, respectively. The black-hole formation time, t_{BH} , for model A4 with $D_T = 0.0625$ is 1.1×10^5 s, and hence, t_{BH} depends strongly on the initial perturbation. (However, the final outcomes of the collapse depend only weakly on the initial perturbation: see below.)

After the black-hole formation, the mass accretion onto the black hole continues subsequently for ≈ 100 – 1000 s, and the accretion terminates at $t - t_{\text{BH}} \approx 300$ s, 70 s, 800 s, and 150 s for models A1–A4, respectively. To specify the mass which is not absorbed by the black hole, we define M_{ter} as the value of M_{total} at the time at which the accretion to the black hole terminates. We list M_{ter} together with the mass (M_{BH}) and dimensionless spin parameter (a_{BH}) of the final state of the black holes in Table II. Approximately 0.5% of the initial mass is located outside the black hole at the final state for models A1 and A2. On the other hand, these values are 5% for rapidly rotating models A3 and A4, respectively. The values of the dimensionless spin parameter, a_{BH} , are ≈ 0.5 for models A1 and A2 and ≈ 0.7 for rapidly rotating models A3 and A4, respectively.

We find that the accretion for hydrogen-burning models A1 and A3 occurs more slowly than helium-burning models A2 and A4. This is caused by the fact that the SMS core density (and spacetime curvature) for models A1 and A3 are lower than for models A2 and A4. The curves for model A4 with $D_T = 0.5$ and 0.0625 show that the property of the accretion of the mass to the formed black hole depends only weakly on D_T . This is due to the fact that after the formation of the black hole, the accreting matter is approximately in free fall, and thus, the property of the accretion of the mass does not depend strongly on the initial perturbation. The mass of the torus depends strongly on the initial specific angular momentum distribution of the SMS core (see Sec. III D).

Figure 3 shows the time evolution of the mass ejected from the domain $\sqrt{X^2 + Z^2} < D$, $M_{\text{eje}}(D, t)$, defined by Eq. (B12). We set $D = 600R_M$ and define

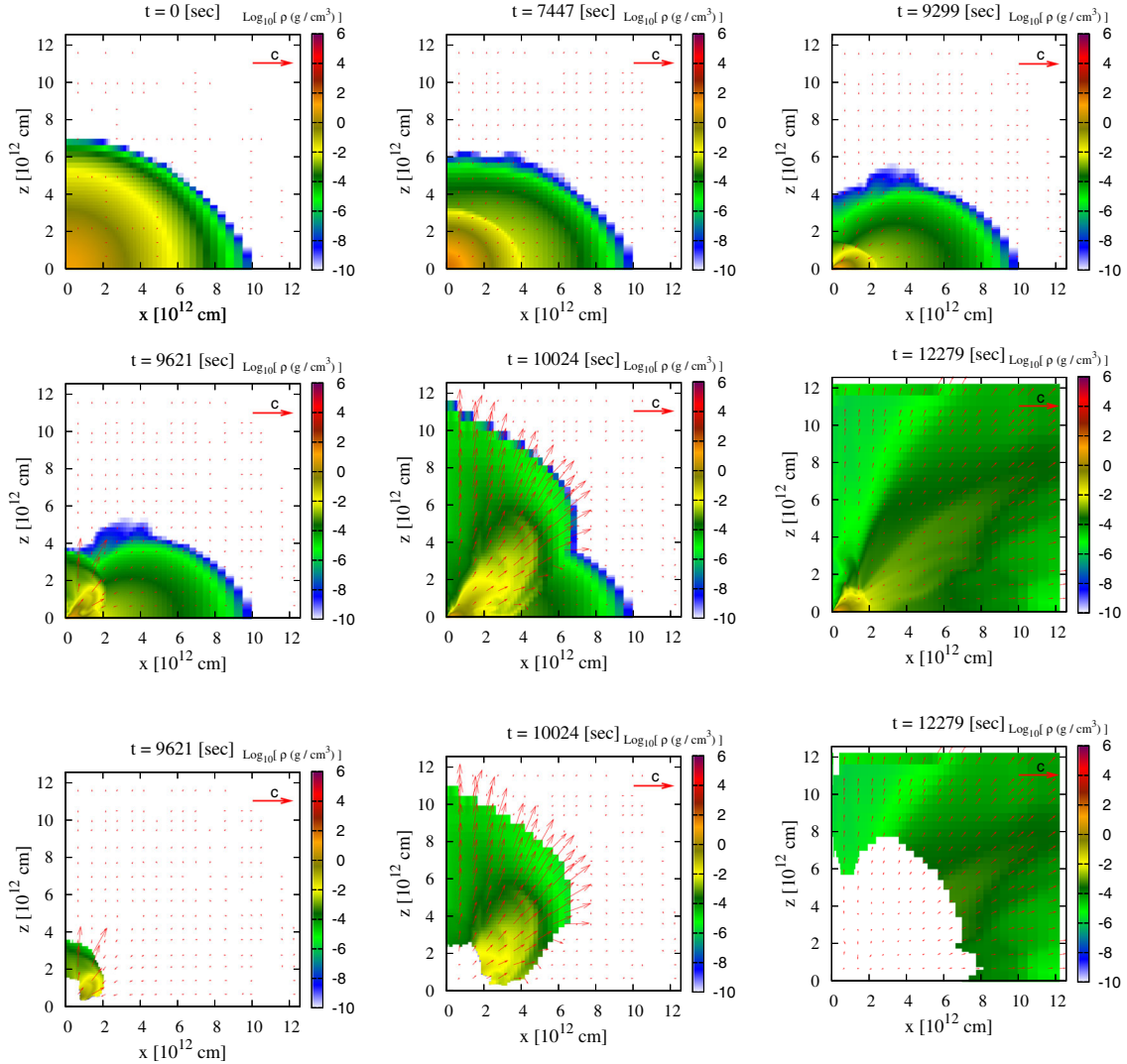


FIG. 1. Snapshots of density profiles during the SMS core collapse for model A4. The 7th–9th panels show only unbound material. The red arrows denote the velocity profile, u^i/u^i ($i = X, Z$), which are normalized as indicated in the upper right-hand corner of each snapshot.

$M_{\text{eje}}(D) \equiv M_{\text{eje}}(D, t = t^*)$ where t^* is the time at which all of the fluid elements of the outflow finish escaping from the domain $\sqrt{X^2 + Z^2} < D$. We find that $M_{\text{eje}}(D)$ depends only weakly on D as long as $D \geq 600R_{\text{M}}$, and thus, we omit the argument D in M_{eje} in the following. It is found that M_{eje}/M_0 is approximately 0.2% for models A1 and A2 and 1% for rapidly rotating models A3 and A4, respectively. The outflow is driven by a purely hydrodynamical effect (see Sec. IV A). Thus M_{eje} is approximately 1/5 times smaller than M_{ter} .

Unlike M_{ter} , the total mass of the outflow for model A4 with $D_{\text{T}} = 0.0625$ is approximately 70% of that for model with $D_{\text{T}} = 0.5$. We will discuss the reason for this as well as the property of the outflow in detail in Sec. IV (see also Appendix C for a method to take $D_{\text{T}} = 0$ limit for the outflow).

We also explored the gravitational collapse of non-rotating SMSs with the same initial chemical composition as for models A1 and A2, and found that for both of them a BH with no surrounding torus is formed. Outflow was not also found. These results are consistent with previous studies [36–38]. In Ref. [37], they found that when a nonrotating SMS of special mass becomes gravitationally unstable in the helium-burning phase, it would explode due to helium-burning. However, the mass range for which a SMS could explode is very narrow (core mass $\approx 30500 M_{\odot}$ and total mass $\approx 55500 M_{\odot}$), and our initial condition is out of this range (core mass $\approx 31300 M_{\odot}$). Thus, our result does not contradict with that in Ref. [37].

Before closing this subsection, we remark the convergence property of the numerical results. Figures 2 and 3 show a good convergence of the numerical result for model A4 among the low, middle, and high resolution results. We

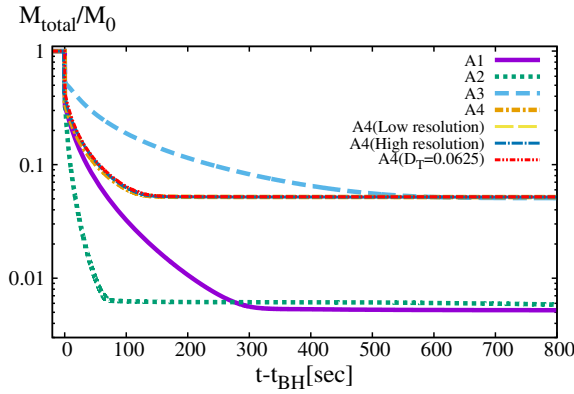


FIG. 2. Time evolution of the total mass located outside the formed black hole. The purple-solid, green-dotted, light-blue-dashed, and orange-dashed-dotted curves denote the results for models A1–A4 with $D_T = 0.5$, respectively. The yellow-long-dashed and blue-long-dashed-dotted curves are for model A4 with low and high grid resolutions, respectively. The red-dashed-dotted-dotted curve is for model A4 with $D_T = 0.0625$. t_{BH} is the time of the black-hole formation.

check that for models A1 and A4, the values of M_{total} at $t - t_{\text{BH}} = 2000$ s and M_{ej} agree with each other among the low, middle, and high-resolution cases within 1.5% disagreement.

B. Nuclear and neutrino interaction rate

Figures 4 and 5 display the time evolution of the averaged mass fraction of ^{12}C defined by $\langle Z_C \rangle = M_C/M_{\text{total}}$ for hydrogen-burning models A1 and A3 (Fig. 4) and helium-burning models A2 and A4 (Fig. 5), respectively. Here, $M_C(t)$ denotes the total carbon mass located outside the black hole defined by

$$M_C(t) \equiv \int_{V'} \rho_{0*} Z_C dV. \quad (3.2)$$

Figure 4 shows that $\langle Z_C \rangle$ increases exponentially with time just before the formation of a black hole, but most of them are absorbed into the formed black hole. For both models A1

and A3, the value of $\langle Z_C \rangle$ at $t - t_{\text{BH}} = 2000$ s is at most several tens of times larger than the initial values and mass fractions of protons and heliums are approximately constant throughout the collapse. Figure 5 shows that several tens percent of heliums are burned into carbons just before the black-hole formation, but again almost all of them are absorbed into the formed black hole and the torus is composed primarily of heliums.

Figures 4 and 5 show that the nuclear burning more strongly occurs for slowly rotating models A1 and A2 than for rapidly rotating models A3 and A4. This fact can be understood in the following manner. First, if a SMS core is rapidly rotating, the mass for the SMS core to become unstable to the gravitational collapse is heavier than the slowly rotating models because rotation strongly stabilizes the SMS core against gravitational collapse. We note that the density of the collapsing core just before the black hole formation is smaller for the larger mass model because the length scale of the system is proportional to the mass of the black hole, M_{BH} . Since the gravitational collapse proceeds approximately adiabatically, the temperature is also an increasing function of density. Hence for the lighter SMS core, the density and temperature at the moment of the black-hole formation are higher than for the heavier SMS core, and hence, the lighter SMS core induces stronger nuclear burning.

Figure 6 displays the time evolution of the total energy generation rate of the nuclear burning, \dot{E}_{nuc} , defined by

$$\dot{E}_{\text{nuc}}(t) \equiv \int_{V'} \rho_{0*} (\dot{q}_{\text{CNO}} + \dot{q}_{3\alpha}) dV. \quad (3.3)$$

This rate exponentially increases just before the black-hole formation. We also find that for models A1 and A3, \dot{E}_{nuc} is dominated by CNO cycle both before and after the collapse, and only just before the collapse, the energy generation rate by CNO cycle and triple-alpha reactions are comparable.

Figure 7 displays the time evolution of the total energy loss rate by neutrino, \dot{E}_{ν} , defined by

TABLE II. Quantities for the gravitational collapse of SMS cores. M_{05} : initial mass of SMS cores in units of $10^5 M_{\odot}$. M_{BH5} and a_{BH} : mass in units of $10^5 M_{\odot}$ and spin of the remnant black hole. M_{ter3} : The total mass located outside the black hole after the termination of the mass accretion to the black hole in units of $10^3 M_{\odot}$. E_{tor} : internal energy of the torus. \dot{E}_{nuc} and \dot{E}_{ν} : nuclear energy generation rate and neutrino generation rate of the torus. T_{max} and ρ_{max} : the maximum temperature and density of the torus. τ_{nuc} and τ_{dyn} : heating time scales by nuclear burning and dynamical time (rotation period at the density maximum of the torus). These values are calculated at $t - t_{\text{BH}} = 2000$ s.

Model	M_{05}	M_{BH5}	$a_{\text{BH}}/M_{\text{BH}}$	M_{ter3}	$E_{\text{tor}}[\text{erg}]$	$\dot{E}_{\text{nuc}}[\text{erg/s}]$	$\dot{E}_{\nu}[\text{erg/s}]$	$T_{\text{max}}[10^8\text{K}]$	$\rho_{\text{max}}[\text{g/cm}^3]$	$\tau_{\text{nuc}}[\text{s}]$	$\tau_{\text{dyn}}[\text{s}]$
A1	1.99	1.98	0.50	1.0	1×10^{55}	1×10^{45}	1×10^{37}	4.2	20	1×10^{10}	110
A2	0.470	0.467	0.51	0.29	4×10^{54}	4×10^{46}	3×10^{43}	9.3	400	9×10^7	25
A3	6.56	6.23	0.69	33	7×10^{56}	1×10^{46}	1×10^{43}	5.2	22	7×10^{10}	190
A4	1.57	1.49	0.69	8.2	2×10^{56}	1×10^{48}	3×10^{47}	10	400	2×10^8	46

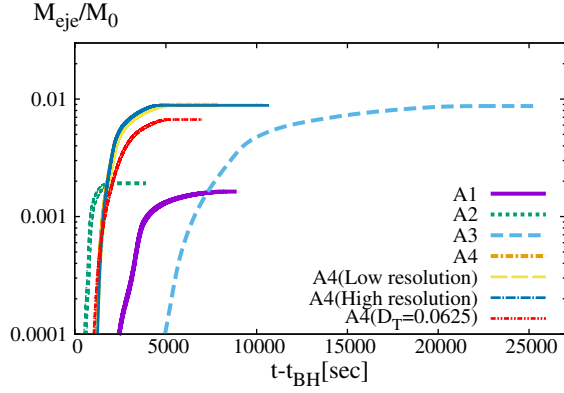


FIG. 3. Time evolution of $M_{\text{ejc}}(D, t)$, the unbound mass ejected from the domain of $\sqrt{X^2 + Z^2} < D$ defined by Eq. (B12). We set $D = 600R_M$. The purple-solid, green-dotted, light-blue-dashed, and orange-dashed-dotted curves denote the results for models A1–A4 with $D_T = 0.5$, respectively. The yellow-long-dashed and blue-long-dashed-dotted curves are for model A4 with low and high grid resolutions, respectively. The red-dashed-dotted-dotted curve is for model A4 with $D_T = 0.0625$. t_{BH} is the time of the black-hole formation.

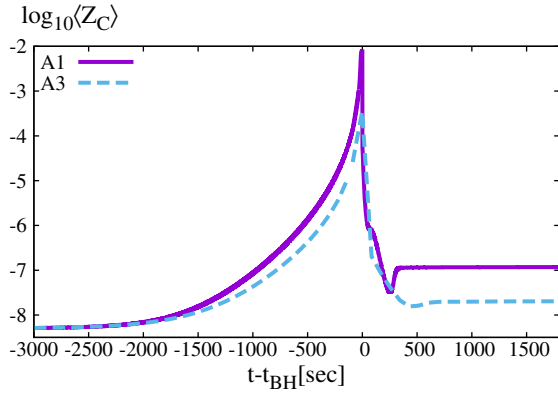


FIG. 4. Time evolution of the averaged mass fraction of carbon for the matter located outside the black hole for hydrogen-burning models A1 (purple-solid) and A3 (light-blue-dashed).

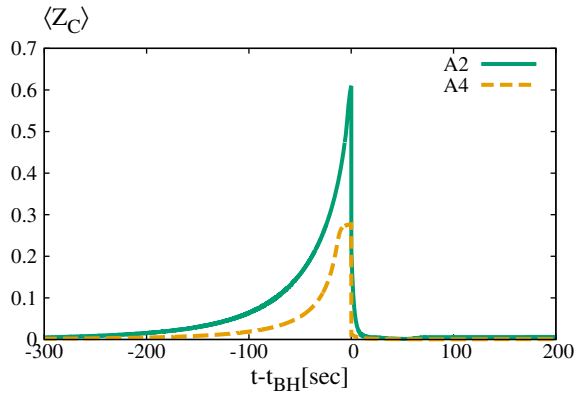


FIG. 5. Time evolution of the averaged mass fraction of carbon for the matter located outside the black hole for helium-burning models A2 (green-solid) and A4 (orange-dashed).

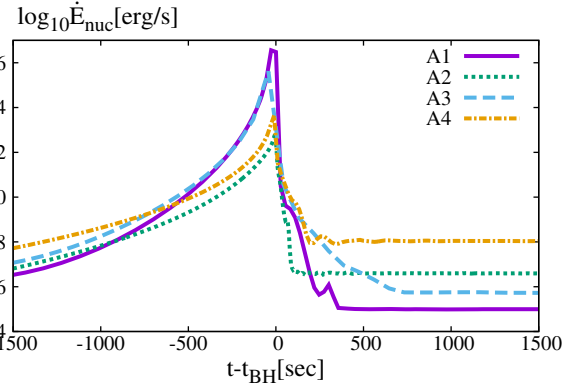


FIG. 6. Time evolution of the total energy generation rate of nuclear burning for the matter located outside the black hole for models A1 (purple-solid), A2 (green-dotted), A3 (light-blue-dashed), and A4 (orange-dashed-dotted), respectively.

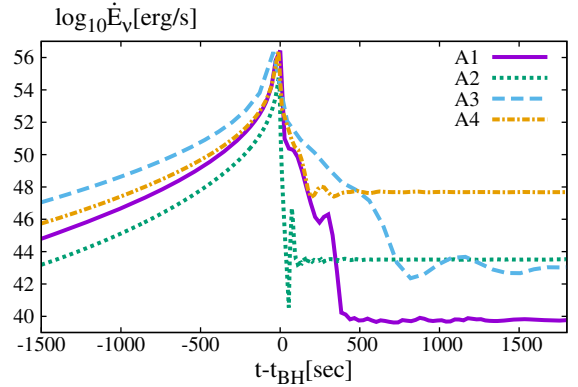


FIG. 7. Time evolution of the neutrino generation rate for the matter located outside the black hole for models A1 (purple-solid), A2 (green-dotted), A3 (light-blue-dashed), and A4 (orange-dashed-dotted), respectively.

$$\dot{E}_\nu(t) \equiv \int_V \rho_{0*} (\dot{q}_{\text{photo}} + \dot{q}_{\text{pair}} + \dot{q}_{\text{plasma}}) dV, \quad (3.4)$$

where \dot{q}_{photo} , \dot{q}_{pair} , and \dot{q}_{plasma} are the neutrino generation rates resulting from the photo-neutrino process, pair-neutrino process, and plasma-neutrino process, respectively. We note again that the effect of neutrino cooling is not included in our simulations.

In the early phase of the collapse, \dot{E}_ν is dominated by the photo-neutrino emission for all the models. Just before the black-hole formation, \dot{E}_ν is dominated by the pair-neutrino emission for all the models. After the collapse, \dot{E}_ν is dominated by the photo-neutrino emission for model A1 and by the pair-neutrino emission for models A2–A4.

\dot{E}_{nuc} and \dot{E}_ν in Table II show the values for models A1–A4 at $t - t_{\text{BH}} = 2000$ s. These values approximately denote the nuclear burning and neutrino cooling rates of the torus. We find that for both \dot{E}_{nuc} and \dot{E}_ν , rapidly rotating

models A3 and A4 have larger values than the slowly rotating models A1 and A2, respectively. In addition, helium-burning models A2 and A4 have larger rates than hydrogen-burning models A1 and A3: The former is due to the fact that for the rapidly rotating models, their tori are more massive than the slowly rotating models as discussed above. The latter is due to the fact that for the helium-burning models, their density and temperature are higher than for the hydrogen-burning models. We list the maximum density, ρ_{\max} , and maximum temperature, T_{\max} , of the torus at $t - t_{\text{BH}} = 2000$ s for models A1–A4 in Table II. The maximum temperature and density for helium-burning models A2 and A4 are approximately 2 and 20 times larger than for hydrogen burning models A1 and A3, respectively.

In Table II, we also list the internal energy of the torus, E_{tor} , heating time scale of the torus by nuclear burning, τ_{nuc} , and rotation period at the density maximum of the torus, τ_{dyn} at $t - t_{\text{BH}} = 2000$ s for models A1–A4, respectively. Here, E_{tor} is defined by

$$E_{\text{tor}}(t) \equiv \int_{V'} \rho_* \epsilon dV, \quad (3.5)$$

where $\rho_* \equiv \rho \sqrt{-g} c u^t$. We calculate τ_{nuc} by $\tau_{\text{nuc}} = E_{\text{tor}} / \dot{E}_{\text{nuc}}$. τ_{nuc} for models A1–A4 is approximately 1×10^{10} s, 9×10^7 s, 7×10^{10} s, and 2×10^8 s, respectively. Hence, the nuclear reaction time scales is much longer than the dynamical time scale of the torus.

Before closing this section, we consider the possible effect of viscosity, which is not taken into account in our present study but it could play an important role for the evolution of the torus surrounding the black hole in reality. In the α -viscous model [52], the viscous heating timescale is written approximately as

$$\tau_{\text{vis}} \sim \alpha^{-1} \tau_{\text{dyn}}. \quad (3.6)$$

With the values of τ_{dyn} listed in Table II, τ_{vis} is $110\alpha^{-1}$ s, $25\alpha^{-1}$ s, $190\alpha^{-1}$ s, and $46\alpha^{-1}$ s for models A1–A4, respectively. This suggests that the viscous heating time scale would be much shorter than the nuclear heating timescale unless $\alpha < 10^{-6}$ for all the models. We also note that the accretion time scale of the torus is the same order as the viscous heating time scale. Thus if we want to predict the long-term evolution of the torus, the viscous effect has to be taken into account.

C. Effects of nuclear burning

The SMS cores do not explode for all the models. For comparison, we also perform simulations for the same initial conditions as models A1–A4 but putting out nuclear burning. We find that the difference of the values of M_{BH} , a_{BH} , E_{tor} , T_{\max} , and ρ_{\max} between these models and models A1–A4 are less than 1%. In this section, we clarify

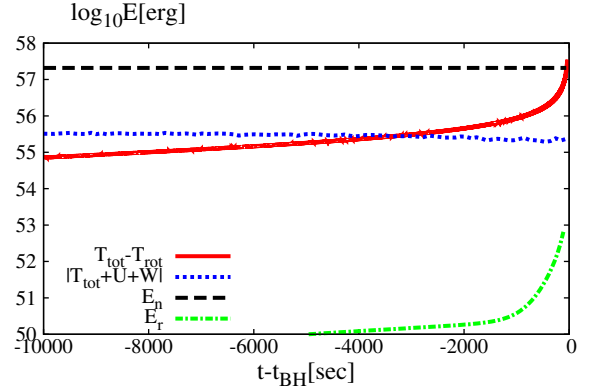


FIG. 8. Time evolution of several key energies for model A1. T_{tot} , T_{rot} , U , W , E_{n} , and E_{r} denote the total kinetic energy, the rotational kinetic energy, the total internal energy, the total gravitational energy, the total rest-mass energy which could be released by nuclear burning, and the total released rest-mass energy by nuclear burning, respectively. We plot $T_{\text{tot}} - T_{\text{rot}}$ (red-solid), $|T_{\text{tot}} + U + W|$ (blue-dotted), E_{n} (black-dashed), and E_{r} (green-dashed-dotted), respectively.

the reason why the nuclear burning does not play an important role during the collapse for our models.

First, we pay attention to the evolution of various energies in the gravitational collapse. Figure 8 plots the evolution of the total kinetic energy, T_{tot} , the rotational kinetic energy, T_{rot} , the total internal energy, U , the total gravitational energy, W , the total rest-mass energy which could be released by nuclear burning, E_{n} , and the total released rest-mass energy by nuclear burning, E_{r} , for model A1, respectively. Here, T_{tot} , T_{rot} , U , and W are defined by

$$T_{\text{tot}}(t) \equiv \int_V \frac{1}{2} \rho_{0*} c^2 (1 - (\alpha c u^t)^2) dV, \quad (3.7)$$

$$T_{\text{rot}}(t) \equiv \int_V \frac{1}{2c} \rho_{0*} h_0 v^\varphi u_\varphi dV, \quad (3.8)$$

$$U(t) \equiv \int_V \rho_* \epsilon dV, \quad (3.9)$$

$$W(t) \equiv M_{\text{ADM}}(t) c^2 - M_{\text{total}}(t) c^2 - T_{\text{tot}}(t) - U(t), \quad (3.10)$$

and M_{ADM} is the ADM mass (gravitational mass) defined by

$$M_{\text{ADM}}(t) \equiv \frac{c^2}{16\pi G} \int_V \left[-\tilde{R} + \frac{16\pi G}{c^4} \rho_h \psi^5 + \psi^{-7} \bar{A}^{ij} \bar{A}_{ij} - \frac{2}{3} \psi^5 K^2 \right] dV. \quad (3.11)$$

Here, $\psi = \rho_g^{-1/2}$, $\bar{A}^i_j \equiv \psi^6 \tilde{A}^i_j$, $\rho_h \equiv \rho h (\alpha c u^t)^2 - P$, and \tilde{R} is the Ricci scalar with respect to $\tilde{\gamma}_{ij}$, respectively. The definition of T_{rot} is equivalent to Eq. (2.40). $T_{\text{tot}} - T_{\text{rot}}$

approximately denotes the kinetic energy associated with the infalling motion. E_n and E_r are defined by

$$E_n(t) \equiv \left(\frac{m_C}{12} - m_p - \frac{m_e}{2} \right) \frac{M_{\text{total}}(t)c^2}{m_p} Y_p(t) + \left(\frac{m_C}{3} - m_\alpha \right) \frac{M_{\text{total}}(t)c^2}{m_\alpha} X_\alpha(t), \quad (3.12)$$

$$E_r(t) \equiv E_n(0) - E_n(t), \quad (3.13)$$

respectively. We find that until the black-hole formation, $T_{\text{tot}} - T_{\text{rot}} \gg E_r$ is satisfied. This fact implies that the nuclear burning cannot halt the collapse of the infalling matter. It is also found that $T_{\text{tot}} - T_{\text{rot}} > E_n$ is satisfied at $t - t_{\text{BH}} \approx 0$ s. This fact indicates that after this time, nuclear reactions cannot induce explosion. We note that for models A2A4, the relations $T_{\text{tot}} - T_{\text{rot}} \gg E_r$ and $T_{\text{tot}} - T_{\text{rot}} > E_n$ for $t - t_{\text{BH}} \approx 0$ s are satisfied. Thus, for any models employed in this paper, the collapse to black holes cannot be halted by the nuclear burning.

Next, we consider the property of the torus. As described in Sec. III B, the nuclear heating time scale is $\gtrsim 10^8$ s for all the models employed in this paper. By contrast, we find that the time scale of the formation of the torus is $\lesssim 10^4$ s for all the models. This is much shorter than the nuclear heating time scale. Hence the nuclear burning does not modify the property of the torus during the gravitational collapse.

Finally, we note that the nuclear burning does not play a role for the outflow. The outflow is initially driven as a result of the shock heating on the surface of the torus. Here, the density and temperature in the shock are not high enough to significantly enhance nuclear burning even at its formation. Hence the nuclear burning does not affect the outflow. We describe the formation process of the outflow in detail in Sec. IV.

D. Torus mass

As we found in the previous section, the effect of nuclear burning only weakly affects the collapse dynamics and the properties of the torus and outflow. Then we search for the relation between M_{ter} and $T_{\text{rot}}/|W|$ for given adiabatic constants neglecting nuclear burning. For this purpose, we performed simulations for additional initial conditions (hereafter referred to as N models). The initial conditions are chosen taking into account the following facts: The red and blue crosses in Fig. 9 show that the values of Γ and $T_{\text{rot}}/|W|$ for models A1–A4 have the relation of $\Gamma = 1.334$ – 1.336 for $T_{\text{rot}}/|W| = 0.002$ – 0.009 . Then we uniformly select 15 initial conditions including 3 different adiabatic constants $\Gamma = 1.334$, 1.335 , and 1.336 and 5 different rotation parameters $T_{\text{rot}}/|W| = 0.002$, 0.004 , 0.006 , 0.008 , and ≈ 0.009 with the same EOS as Eq. (2.21). The open circles in Fig. 9 denote these models.

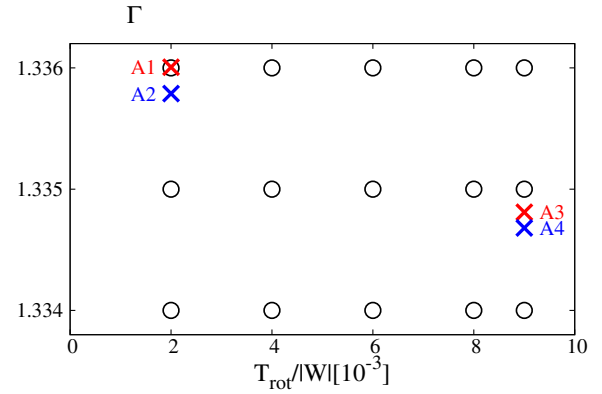


FIG. 9. Initial values of Γ and $T_{\text{rot}}/|W|$ for the hydrogen-burning models (red crosses), the helium-burning models (blue crosses), and the N models (open circles). The crosses correspond to models A1–A4.

The simulation is performed with $D_T = 0.5$. As we already found, the properties of the formed black hole and the mass of the torus depend only weakly on the value of D_T .

We define the mass of the final state of the torus by

$$M_{\text{tor}} \equiv M_{\text{ter}} - M_{\text{eje}}. \quad (3.14)$$

As we found in Sec. III A, M_{eje} is much smaller than M_{ter} , and then, M_{tor} can be approximated by M_{ter} . Figures 10 and 11 depict the dimensionless spin parameter of the remnant black holes and M_{ter} , respectively. The filled circles, squares, and triangles are the results of the numerical simulation and the solid, dashed, and dotted curves denote the relations obtained by the analytical predictions of Ref. [30] for $\Gamma = 1.334$, 1.335 , and 1.336 , respectively.

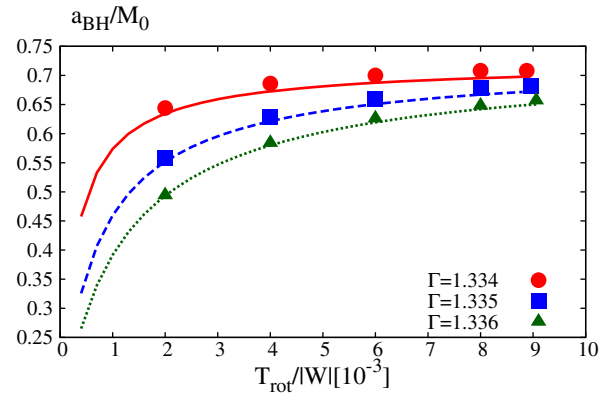


FIG. 10. The dimensionless spin parameter of the remnant black hole as a function of the rotation parameter $T_{\text{rot}}/|W|$ for three values of the adiabatic constant Γ . The filled circles, squares, and triangles are the results of the numerical simulation and the solid, dashed, and dotted curves are the analytical predictions of Ref. [30] for $\Gamma = 1.334$, 1.335 , and 1.336 , respectively.

In Ref. [30], we inferred the mass and spin of the remnant black holes only from the initial conditions in the following manner. First, we employed three assumptions that (i) the collapse proceeds in an axisymmetric manner, (ii) the angular momentum transport due to the viscosity is negligible, and (iii) nuclear burning does not halt the collapse. The first and second assumptions are the same as those we employed in the simulations. The third assumption is shown to be appropriate in Sec. III C.

We also assumed that the gravitational collapse proceeds in the following manner. First, a seed black hole is formed at the center of the collapsing SMS core and it dynamically grows while sequentially absorbing fluid elements from lower values of specific angular momentum, j , defined by

$$j \equiv h_0 u_\varphi. \quad (3.15)$$

We then calculated the mass and angular momentum of the hypothetically growing black hole at each moment by calculating Eqs. (37) and (38) of Ref. [30] and subsequently got the dimensionless spin parameter of the black hole.

Then, assuming that the black hole is Kerr black hole, we can calculate j_{ISCO} by using Eq. (2.21) of Ref. [53]. Here j_{ISCO} is the specific angular momentum, which is needed for a test particle to rotate at an innermost stable circular orbit (ISCO) in the equatorial plane around the black hole. We assumed that the growth of the black hole would terminate at the moment at which j becomes larger than j_{ISCO} . In this assumption, we neglect the pressure and geometry of the torus because j_{ISCO} is determined by calculating the geodesic equation of test particles moving in the equatorial plane.

Figure 10 shows that the dimensionless spin parameter matches well with the prediction, but Fig. 11 shows that M_{ter} is slightly overestimated in the analytic prediction. This is likely due to the fact that each fluid element of the

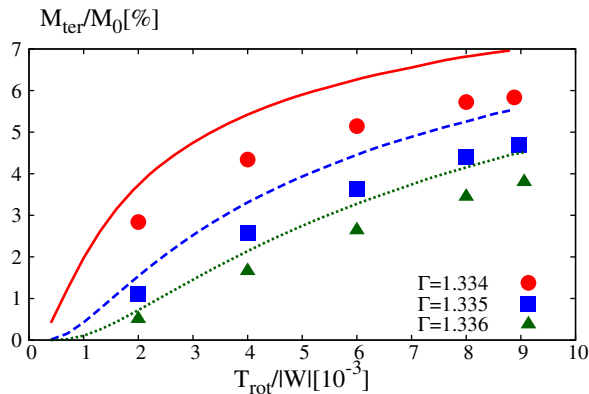


FIG. 11. M_{ter} as a function of $T_{\text{rot}}/|W|$ for three values of adiabatic constant Γ . The filled circles, squares, and triangles are the results of the numerical simulation and the solid, dashed, and dotted curves are the analytic predictions of Ref. [30] for $\Gamma = 1.334, 1.335,$ and 1.336 , respectively.

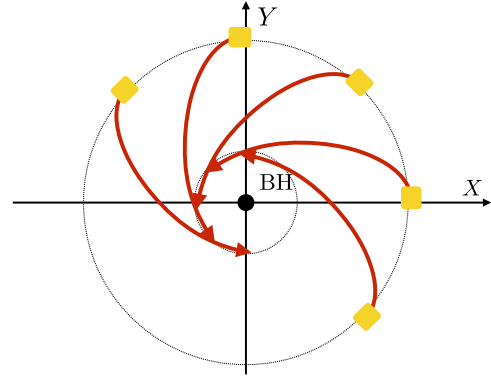


FIG. 12. The sketch of the falling fluid elements (yellow squares) to the formed black hole in the equatorial plane. Even though each fluid element has an elliptical orbit, the axial symmetry is totally satisfied.

SMS core falls toward the black hole with an elliptical orbit, and then, some fluid elements fall into the black hole even when their specific angular momentum is larger than j_{ISCO} . [Even though each fluid element has an elliptical orbit, the axial symmetry is totally satisfied (see Fig. 12).] The pressure and geometry of the torus may also affect the result. Nevertheless, the analytic calculation predicts the mass of the torus within 30% error.

We conclude that if a SMS core is rotating with $T_{\text{rot}}/|W| \gtrsim 0.002$, (i) a few percent of the initial mass forms a torus surrounding the central black hole irrespective of the nuclear burning phases of SMS cores, and (ii) the dimensionless spin of the remnant black hole is in the range between ≈ 0.5 and 0.7 .

We should clarify the reason why the dimensionless spin parameter of the formed black hole does not depend strongly on the value of $T_{\text{rot}}/|W|$. The direct reason for this is that the dimensionless spin parameter of marginally stable SMS depends weakly on the value of $T_{\text{rot}}/|W|$. Thus, we describe the reason for this in the following.

As we showed in Ref. [30], the compactness of marginally stable SMS increases (approximately) linearly with the increase of $T_{\text{rot}}/|W|$ [see Eq. (2.45)]. Here, for rigidly rotating SMS, $T_{\text{rot}} = I\Omega^2/2 = J_K^2/2I$ and $|W| \approx 3M_0^2/2R$ where I denotes the moment of inertia and R denotes the equatorial stellar radius. Thus, we have

$$\frac{T_{\text{rot}}}{|W|} \approx \left(\frac{RM_0^2}{3I} \right) \left(\frac{J_K}{M_0^2} \right)^2. \quad (3.16)$$

Because I is proportional to $M_0 R^2$, $RM_0^2/I \propto M_0/R$, and thus, $J_K/M_0^2 \propto (T_{\text{rot}}/|W|)^{1/2} (R/M_0)^{1/2}$. As we already mentioned above, M_0/R increases approximately linearly with the increase of $T_{\text{rot}}/|W|$ for marginally stable SMS. Specifically, Eq. (2.45) gives the following approximate relation

$$\frac{M_0}{R} \propto \Gamma - 4/3 + \frac{2T_{\text{rot}}}{3|W|}. \quad (3.17)$$

Therefore, for $T_{\text{rot}}/|W| \gtrsim 3(\Gamma - 4/3)/2$, the dimensionless spin parameter of marginally stable SMS depends weakly on $T_{\text{rot}}/|W|$.

IV. OUTFLOW

As found in Sec. III, a fraction of the mass of the SMS core is ejected soon after a rotating black hole is formed. In this section, we describe the properties of the outflow in detail. For this analysis, we define several quantities of the outflow in Appendix B.

A. Formation process of the outflow

First, we describe the mechanism to drive the outflow. Figures 13 and 14 display the snapshots of the density and specific entropy profiles at the formation of the torus for the N model with $\Gamma = 1.336$ and $T_{\text{rot}}/|W| \approx 0.009$. For this model, the chemical composition is set to be the same as the hydrogen-burning models and initial value of the specific entropy is $s/k_B \approx 400$.

The 1st panel shows the density and specific entropy profiles at the launch time of the outflow. The fluid elements conserve their specific angular momentum, and hence, if their initial specific angular momentum is slightly larger than j_{ISCO} for the formed black hole, they escape falling into the black hole due to the centrifugal force, and

accrete to the vicinity of ISCO of the black hole. These process are approximately adiabatic, and thus, the torus conserves its specific entropy. At the same time, a fraction of the fluid elements in the torus is pushed inward by the inertia of the entire torus matter which has small infall velocity. Then, the material falling from a high latitude toward the inner edge of the torus hits the inner part of the torus, and, due to the strong encounter among the fluid elements, shocks are formed. As a result, a dense bubble (of a torus shape) is formed by the shock heating at the very central region, i.e., $X < 1 \times 10^{11}$ cm (2nd panel). At this time, the bubble has larger specific entropy due to the shock heating.

The formed bubble immediately expands vertically because the density above the torus is very small (3rd panel). The matter in this bubble is rotating around the z -axis, and thus, feels strong centrifugal force. Hence, it moves toward the surface of the torus. Then most of the fluid components in the bubble is reabsorbed by the main body of the torus. However, a fraction of them which expands vertically can avoid colliding with the torus, and then, it spreads outward (4th–6th panels). This situation is similar to the hot bubble formation in a collapsar model [54]. The formation process of the outflow is also discussed in Ref. [39].

B. Properties of the outflow

Next, we summarize the property of the outflow. Figure 15 shows the time evolution of the total mass M_{outf} (red-solid), the total kinetic energy T_{outf} (blue-dashed),

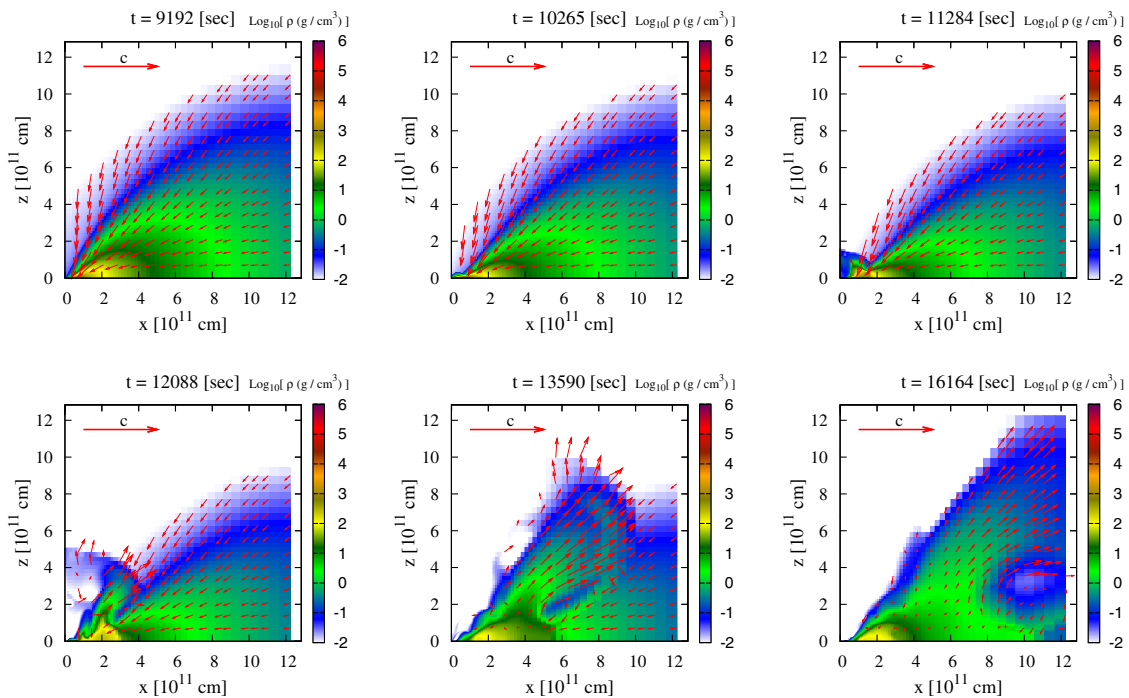


FIG. 13. The density profiles near the formation time of the torus surrounding the black hole. They show zoom-in views of the central region. The red arrows denote the velocity vectors and their length scale is normalized as indicated in the upper left-hand corner of each snapshot. Just after the torus formation, a strong shock and a resulting bubble are formed and a fraction of the torus matter is ejected.

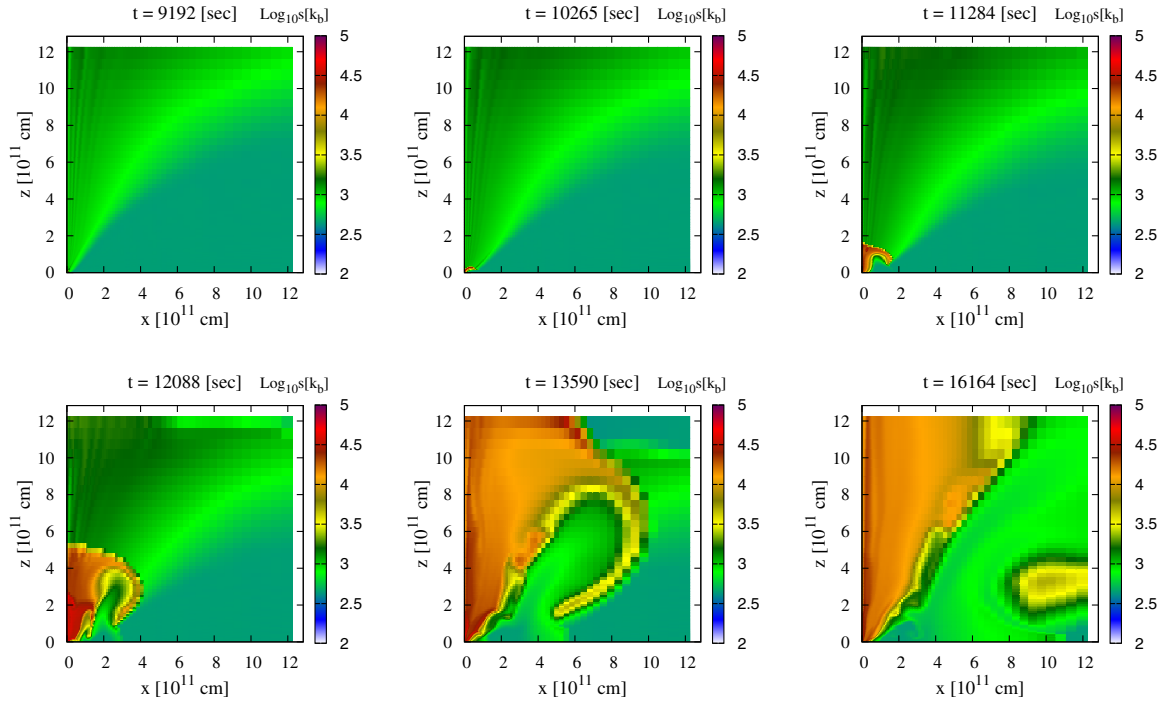


FIG. 14. The total specific entropy profiles near the formation time of the torus surrounding the black hole. They show zoom-in views of the central region. The specific entropy of the SMS core before the onset of the collapse for this model is $s/k_B \approx 400$. Just after the torus formation, a strong shock and a resulting bubble are formed, and thus, the bubble has much larger specific entropy than its initial value.

the radial component of the total kinetic energy T_{oflw}^r (light blue-long-dashed), the total internal energy U_{oflw} (orange-dashed-dotted), the total gravitational potential energy $|W_{\text{oflw}}|$ (green-dotted), and the total energy E_{oflw} (black-long-dashed-dotted) for hydrogen-burning model A3 with $D_T = 0.5$, respectively. They are defined by Eqs. (B14), (B15), (B16), (B17), and (B18). Here, t_g is the light crossing time defined by

$$t_g \equiv \frac{GM_0}{c^3}, \quad (4.1)$$

where M_0 is the initial gravitational mass of the SMS core.

Here, D_T is the initial temperature perturbation parameter defined by Eq. (2.50). We found that the quantities of the outflow depend on the value of D_T . However, we are here interested in the semiquantitative properties of the outflow, and hence, we overlook the quantitative dependence of the outflow properties on the value of D_T . The dependence of the quantities of the outflow on D_T is discussed in Appendix C.

For $t - t_{\text{BH}} \lesssim 1000t_g$, the mass and total energy are increasing because the outflow propagates while sweeping the mass in the outer layer of the SMS core. At $t - t_{\text{BH}} \approx 1000t_g$, most of the outflow matter reaches the surface of the SMS core, and hence, the increase of the mass and total energy becomes slower. The final value of the outflow mass is $\approx 5700 M_\odot$ in this model.

For $t - t_{\text{BH}} \gtrsim 1000t_g$, the total kinetic energy starts decreasing slightly. We speculate that this decrease is due to the following reasons: (i) the fluid elements move in the gravitational potential of the central object, (ii) the shock occurred in the outflow dissipates the kinetic energy of the outflow, and thus, a fraction of the outflow becomes bound again, and (iii) a numerical error induces the decrease of the total energy. The total energy at $t - t_{\text{BH}} = 5000t_g$ is approximately 1.8×10^{56} erg. The possible error size to this would be of order 10^{54} erg as discussed above.

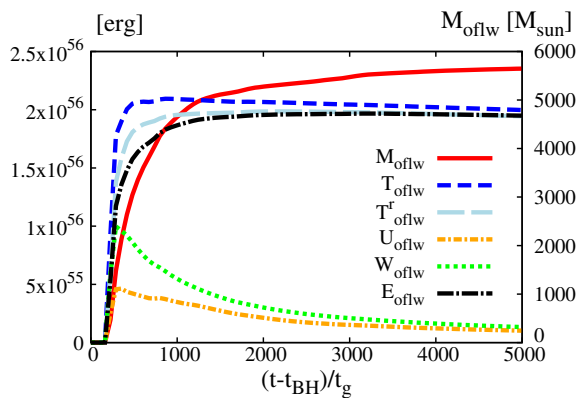


FIG. 15. The time evolution of several key quantities of the outflow for model A3. We plot the total mass of the outflow (red-solid), together with the total kinetic energy (blue-dashed), the radial component of the total kinetic energy (light blue-long-dashed), the total internal energy (orange-dashed-dotted), the total gravitational potential energy (green-dotted), and the total energy (black-long-dashed-dotted), respectively.

The total kinetic energy is approximately 10 times larger than the rotational kinetic energy, internal energy, and gravitational potential energy. This implies that the radial component accounts for most of the total energy. Hence the outflow would propagate through the envelope of the SMS approximately radially. We find that these properties are satisfied for all the models.

The reason why the properties of the outflow do not depend on the chemical composition of the SMS core can be understood in the following manner. As described in Sec. III C, the effect of nuclear burning can be neglected throughout the collapse. If we neglect the effect of nuclear burning, the gravitational collapse proceeds approximately adiabatically before the formation of the shocks. Then, the EOS of the SMS core can be approximated by the polytropic EOS with $\Gamma \approx 4/3$ because the SMS core is radiation pressure dominated. Thus if the same rotation parameter is taken, the dynamics of the gravitational collapse is qualitatively the same irrespective of the chemical composition. After the shock formation, the system becomes no longer adiabatic. However, qualitatively the same collapse may induce qualitatively the same outflow.

Figures 16 and 17 show the time evolution of the total mass and energy of the outflow for models A1–A4. We also list the total mass and energy of the outflow for models A1–A4 at $t - t_{\text{BH}} = 5000t_g$ in Table III. For rapidly rotating models A3 and A4, the total mass and energy of the outflow is larger than for slowly rotating models A1 and A2, respectively. This is due to the following reasons: (i) the initial mass of the SMS core for the rapidly rotating models are heavier than for the slowly rotating models, (ii) for the rapidly rotating models, each fluid element of the SMS core has larger specific angular momentum than for the slowly rotating models, and thus, more fraction of the mass escapes being swallowed by the black hole, and hence, can be ejected by the system due to centrifugal force barrier at the formation of the outflow as described in Sec. IV A.

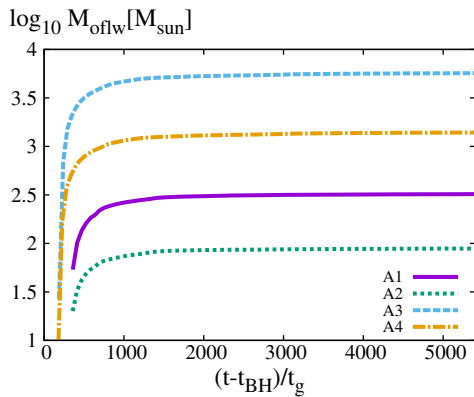


FIG. 16. The time evolution of the total mass of the outflow, M_{oflw} , for models A1 (purple-solid), A2 (green-dotted), A3 (light-blue-dashed), A4 (orange-dashed-dotted), respectively.

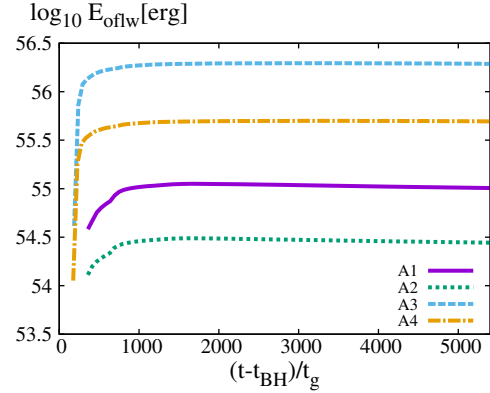


FIG. 17. The time evolution of the outflow energy, E_{oflw} , for models A1 (purple-solid), A2 (green-dotted), A3 (light-blue-dashed), A4 (orange-dashed-dotted), respectively. We note that E_{oflw} would have an error of order 10^{54} erg as discussed in Sec. IV B.

Figures 18 and 19 display the dependence of the mass and energy of the outflow on $T_{\text{rot}}/|W|$ at $t - t_{\text{BH}} = 5000t_g$ for N models. Here, we again choose $D_T = 0.5$. Both the mass and energy of the outflow increase as $T_{\text{rot}}/|W|$ increases while the dependence is weaker for the ejecta energy. For example, for $T_{\text{rot}}/|W| \gtrsim 0.004$, the energy of the outflow is between 0.01% and 0.018% of the initial rest-mass energy. Thus the outflow energy for the SMS core collapse would be typically $\approx 10^{55} (M_0/10^5 M_\odot)$ erg for rapidly rotating models with $T_{\text{rot}}/|W| \gtrsim 0.004$.

Figure 20 denotes the time evolution of the average velocity of the outflow at infinity, $\langle v_{\text{inf}} \rangle$, defined by

$$\langle v_{\text{inf}}(t) \rangle \equiv \sqrt{\frac{2(T_{\text{oflw}} + W_{\text{oflw}})}{M_{\text{oflw}}}}, \quad (4.2)$$

for models A1–A4. At $t - t_{\text{BH}} \gtrsim 3000t_g$, $\langle v_{\text{inf}} \rangle$ converges to $\approx 0.2c$ for all the models. We also find that $\langle v_{\text{inf}} \rangle$ is $\approx 0.2c$ for all N models. Thus the outflow is escaped from the system with a subrelativistic velocity. In reality this outflow is likely to collide with the envelope of SMS surrounding

TABLE III. Total mass and energy of the outflow for models A1–A4 with $D_T = 0.5$. M_{oflw} and E_{oflw} denote the total mass and energy defined by Eq. (B13) at $t - t_{\text{BH}} = 5000t_g$, respectively. We note that E_{oflw} would have an error of order 10^{54} erg as discussed in Sec. IV B. $E_{\text{oflw}}(D_T = 0)$ is the value of E_{oflw} at $t - t_{\text{BH}} = 5000t_g$ with $D_T = 0$ for models A2 and A4 estimated in Appendix C.

Model	$M_{\text{oflw}}(M_\odot)$	$E_{\text{oflw}}(\text{erg})$	$E_{\text{oflw}}(D_T = 0)(\text{erg})$
A1	320	1.0×10^{55}	
A2	90	2.8×10^{54}	2.8×10^{54}
A3	5700	1.8×10^{56}	
A4	1400	4.7×10^{55}	3.1×10^{55}

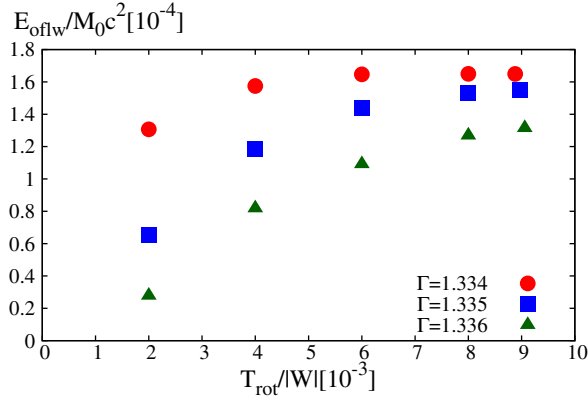


FIG. 18. The relation between E_{oflw} and $T_{\text{rot}}/|W|$ for the N models with $D_T = 0.5$. The filled-circles, squares, and triangles denote the value for $\Gamma = 1.334, 1.335$, and 1.336 at $t - t_{\text{BH}} = 5000t_g$, respectively.

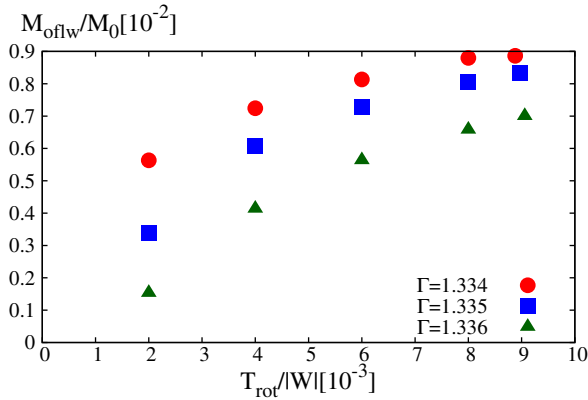


FIG. 19. The relation between M_{oflw} and $T_{\text{rot}}/|W|$ for the N models with $D_T = 0.5$. The filled-circles, squares, and triangles denote the value for $\Gamma = 1.334, 1.335$, and 1.336 at $t - t_{\text{BH}} = 5000t_g$, respectively.

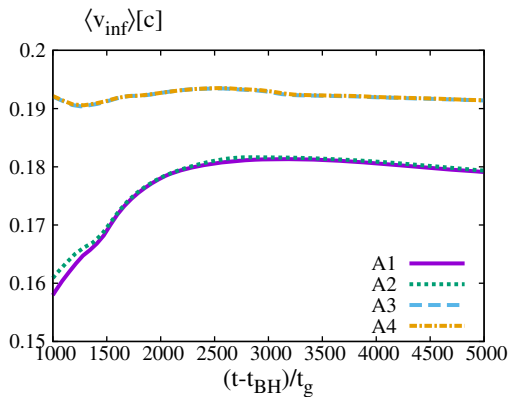


FIG. 20. The time evolution of the average velocity, $\langle v_{\text{inf}} \rangle$, for models A1 (purple-solid), A2 (green-dotted), A3 (light-blue-dashed), A4 (orange-dashed-dotted), respectively.

its core region. It will be interesting to explore the phenomena associated with this collision in a future work.

Finally, we briefly mention the angular dependence of the outflow. The outflow is ejected approximately isotropically. However, the amount of the total mass and energy of the outflow are small near the rotational axis and the equatorial plane. This is due to the fact that the centrifugal force barrier and the torus prevent the outflow from propagating to the rotational axis and the equatorial plane, respectively.

We conclude that the total energy of the outflow is 10^{54-56} erg and approximately dominated by the radial component of the total kinetic energy, with the average velocity of the outflow $\approx 0.2c$ irrespective of the initial chemical composition and rotation of the SMS core.

V. DISCUSSION

A. Estimation for the luminosity of the outflow

After its ejection, the outflow would collide with the envelope of the SMS. In this section, we estimate the luminosity after the gravitational collapse following the derivation of the one-zone analytical light curves of cocoon emission discussed in Ref. [35].

When the outflow collides with the envelope, the envelope would get the kinetic energy and start expanding. The average velocity of the envelope could be estimated by

$$v_{\text{exp}} \approx \sqrt{\frac{2E_{\text{exp}}}{M_{\text{env}}}} \approx 3.2 \times 10^8 \text{ cm/s} \left(\frac{E_{\text{exp}}}{10^{55} \text{ erg}} \right)^{\frac{1}{2}} \left(\frac{M_{\text{env}}}{10^5 M_{\odot}} \right)^{-\frac{1}{2}}, \quad (5.1)$$

where E_{exp} and M_{env} are the total energy of the outflow and the mass of the envelope of the SMS, respectively.

By using the first law of thermodynamics, the thermal evolution of the envelope could be described by

$$\frac{dE_{\text{int}}}{dt} = -P \frac{dV}{dt} - L, \quad (5.2)$$

where E_{int} , L , P , and V are the total internal energy, the luminosity, the pressure, and the volume of the envelope, respectively. We assume that the envelope is radiation pressure dominated, i.e., $E_{\text{int}} = 3PV$. In the following estimation, we ignore the heating source of the envelope.

By using the diffusion approximation, the luminosity of the surface of the SMS could be written by

$$L \approx 4\pi R^2 \frac{c}{\kappa \rho} \frac{\partial P}{\partial r} \approx \frac{4\pi c R E_{\text{int}}}{3\kappa M_{\text{env}}}, \quad (5.3)$$

where ρ , κ , and R are the density, the opacity and the radius of the envelope given by

$$R(t) = R_0 + v_{\text{exp}} t, \quad (5.4)$$

respectively. Here, R_0 is the initial radius of the envelope.

Using Eqs. (5.3) and (5.4), we get the relation between L and E_{int}

$$L = \frac{t + t_e}{t_d^2} E_{\text{int}}, \quad (5.5)$$

where t_e and t_d are the expansion time and diffusion time defined by

$$t_e \equiv \frac{R_0}{v_{\text{sh}}} \approx 3.2 \times 10^5 \text{ s} \left(\frac{R_0}{10^{14} \text{ cm}} \right) \left(\frac{E_{\text{exp}}}{10^{55} \text{ erg}} \right)^{-\frac{1}{2}} \left(\frac{M_{\text{env}}}{10^5 M_\odot} \right)^{\frac{1}{2}}, \quad (5.6)$$

$$t_d \equiv \sqrt{\frac{3\kappa M_{\text{env}}}{4\pi v_{\text{sh}} c}} \approx 1.3 \times 10^9 \text{ s} \left(\frac{E_{\text{exp}}}{10^{55} \text{ erg}} \right)^{-\frac{1}{4}} \left(\frac{M_{\text{env}}}{10^5 M_\odot} \right)^{\frac{3}{4}}, \quad (5.7)$$

respectively. Here, we use $\kappa = 0.35 \text{ g/cm}^2$, which is the Thomson scattering opacity of the primordial chemical composition. Using Eq. (5.5), we can integrate Eq. (5.2) and get the time evolution of the luminosity

$$L(t) = L_0 \exp \left\{ -\frac{1}{2t_d^2} (t^2 + 2t_e t) \right\}, \quad (5.8)$$

where L_0 is the initial luminosity. By Eq. (5.5), L_0 can be given by $L_0 = t_e E_{\text{int}}(0)/2t_d^2$ where $E_{\text{int}}(0)$ is the initial internal energy of the outflow. E_{int} is of order 10^{55} erg . Inserting Eqs. (5.6) and (5.7), we get $L_0 \approx 10^{42} \text{ erg/s}$. However, this luminosity is much smaller than the initial Eddington luminosity of the SMS $L_{\text{Edd}} \approx 10^{43} \text{ erg/s}$ ($M_{\text{SMS}}/10^5 M_\odot$). Here, M_{SMS} is the total mass of the SMS. This fact shows that we cannot observe directly the shock due to the outflow but observe the time evolution of the luminosity due to expanding envelope.

Next, we estimate the time evolution of the luminosity of the expanding envelope. For the expanding envelope, we can get the time evolution of the luminosity by inserting the Eddington luminosity into L_0 . Equation (5.8) shows that the luminosity will gradually decrease with time scale t_d .

When the surface effective temperature drops to $T_{\text{ion}} \approx 6000 \text{ K}$, the hydrogen recombination would occur. We define the time t_{ion} as the moment that the surface effective temperature drops to the critical temperature T_{ion} . Assuming $t_{\text{ion}} \ll t_d$ and $L \approx L_{\text{Edd}}$, t_{ion} and the radius at this moment, R_{ion} , could be estimated by using Eq. (5.4) and $L_{\text{Edd}} = 4\pi R_{\text{ion}}^2 \sigma_{\text{SB}} T_{\text{ion}}^4$ as,

$$t_{\text{ion}} \approx 1.2 \times 10^7 \text{ s} \times \left(\frac{M_{\text{SMS}}}{10^5 M_\odot} \right) \left(\frac{E_{\text{exp}}}{10^{55} \text{ erg}} \right)^{-\frac{1}{2}} \left(\frac{M_{\text{env}}}{10^5 M_\odot} \right)^{\frac{1}{2}}, \quad (5.9)$$

$$R_{\text{ion}} \approx 3.9 \times 10^{15} \text{ cm} \left(\frac{M_{\text{SMS}}}{10^5 M_\odot} \right), \quad (5.10)$$

where σ_{SB} is the Stefan Boltzmann constant. For $t > t_{\text{ion}}$, the radius of photosphere R_{ph} locates on the inside of the surface of the SMS.

We assume that the region with its effective temperature $\gtrsim 6000 \text{ K}$ is fully ionized and the photosphere is formed around the surface with its effective temperature $\approx 6000 \text{ K}$. By using the first law of thermodynamics, we get the time evolution of the radius of the photosphere (see Appendix B of [35])

$$R_{\text{ph}}(t)^2 = v_{\text{sh}}^2 \left\{ t_{\text{ion}}^{\frac{6}{5}} t_{\text{ion}}^{\frac{4}{5}} \left(1 + \frac{t_{\text{ion}}^2}{7t_d^2} \right) - \frac{t^4}{7t_d^2} \right\}. \quad (5.11)$$

R_{ph} takes a maximum value $R_{\text{ph,max}}$ at t_{max} ,

$$t_{\text{max}} \approx \left(\frac{21}{10} \right)^{\frac{5}{14}} t_{\text{ion}}^{\frac{2}{7}} t_d^{\frac{5}{7}} \approx 4.4 \times 10^8 \text{ s} \quad (5.12)$$

$$\times \left(\frac{M_{\text{SMS}}}{10^5 M_\odot} \right)^{\frac{2}{7}} \left(\frac{E_{\text{exp}}}{10^{55} \text{ erg}} \right)^{-\frac{9}{28}} \left(\frac{M_{\text{env}}}{10^5 M_\odot} \right)^{\frac{10}{28}},$$

$R_{\text{ph,max}} \approx 2.9 \times 10^{16} \text{ cm}$

$$\times \left(\frac{M_{\text{SMS}}}{10^5 M_\odot} \right)^{\frac{8}{7}} \left(\frac{E_{\text{exp}}}{10^{55} \text{ erg}} \right)^{\frac{3}{14}} \left(\frac{M_{\text{env}}}{10^5 M_\odot} \right)^{\frac{3}{14}}. \quad (5.13)$$

At this time, the luminosity also takes a maximum value,

$$L_{\text{max}} \approx 4\pi R_{\text{ph,max}}^2 \sigma_{\text{SB}} T_{\text{ion}}^4 \approx 7.5 \times 10^{44} \text{ erg/s} \times \left(\frac{M_{\text{SMS}}}{10^5 M_\odot} \right)^{\frac{16}{7}} \left(\frac{E_{\text{exp}}}{10^{55} \text{ erg}} \right)^{\frac{3}{7}} \left(\frac{M_{\text{env}}}{10^5 M_\odot} \right)^{\frac{3}{7}}. \quad (5.14)$$

This shows that if the collapse of a SMS with mass $10^5 M_\odot$ takes place at $z \approx 10$, the luminosity would become approximately 100 times brighter than its Eddington luminosity at $\approx 10^2 \text{ yrs}$ after the gravitational collapse of the SMS and be kept for $\approx 10^2 \text{ yrs}$.

B. Ringdown gravitational waves associated with the formation of black holes

As we showed in our previous paper [31], bursts gravitational waves are emitted in the formation process of rotating black holes and they can be the sources for LISA [32]. Figure 21 plots gravitational waves $[(l, m) = (2, 0)$

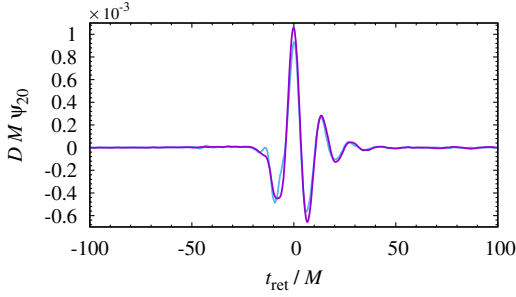


FIG. 21. Gravitational waveforms ($l = 2$ axisymmetric mode of Ψ_4) as a function of retarded time for N models with $\Gamma = 1.335$ and with $T_{\text{rot}}/|W| = 0.004$ (light blue) and $T_{\text{rot}}/|W| \approx 0.009$ (purple).

component of the outgoing component of the complex Weyl scalar] for N models with $\Gamma = 1.335$ and with $T_{\text{rot}}/|W| = 0.004$ and ≈ 0.009 . Note that for $T_{\text{rot}}/|W| \approx 0.009$, the waveform agrees approximately with that shown in our previous paper [31]. This figure illustrates the fact that the gravitational waveforms are characterized primarily by the ringdown oscillation associated with the quasinormal mode of the formed black holes. This feature is found irrespective of the values of Γ and $T_{\text{rot}}/|W|$.

The other important finding is that the amplitude of gravitational waves (and hence the total radiated energy of gravitational waves) does not depend strongly on the values of $T_{\text{rot}}/|W|$ as long as it is of order 10^{-3} (i.e., it is of order $\Gamma - 4/3$). This property is in particular the case for smaller values of Γ . The reason for this is as follows: As described in Sec. III D, the compactness of the marginally stable configuration of SMS depends strongly on the value of $T_{\text{rot}}/|W|$ because the high value of $T_{\text{rot}}/|W|$ contributes significantly to the stabilization against general relativistic instability to radial collapse [30] (specifically, the compactness of the marginally stable SMS with higher values of $T_{\text{rot}}/|W|$ is larger). Reflecting this fact, the dimensionless spin parameter of marginally stable SMS depends weakly on the value of $T_{\text{rot}}/|W|$. This implies that for $T_{\text{rot}}/|W| = O(10^{-3})$, irrespective of the values of $T_{\text{rot}}/|W|$, the SMS has an appreciably nonspherical degree at the formation of black holes, which contributes to the emission of gravitational waves in the black hole formation.

Table IV lists the energy emitted by gravitational waves for all N models. This shows that the total radiated energy,

TABLE IV. $\Delta E/M_0$ in units of 10^{-6} .

$T_{\text{rot}}/ W $	$\Gamma = 1.334$	1.335	1.336
0.002	1.2	0.7	0.5
0.004	1.2	1.0	0.8
0.006	1.2	1.1	1.0
0.008	1.2	1.1	1.1
≈ 0.009	1.2	1.1	1.1

ΔE , is in a narrow range between $5 \times 10^{-7} M_0$ and $1.2 \times 10^{-6} M_0$. We note that the peak amplitude of gravitational waves depends approximately on $\Delta E^{1/2}$. Thus, the dependence of the peak amplitude on $T_{\text{rot}}/|W|$ is even weaker.

In Ref. [31], we pointed out that gravitational waves from the collapse of rapidly rotating SMS can be detected by LISA if the collapse occurs for the cosmological redshift smaller than about 3. The finding in this paper shows that even if the SMS is not rapidly rotating, gravitational waves from the collapse of SMS may be detected by LISA if the value of $T_{\text{rot}}/|W|$ is of $O(10^{-3})$.

C. Possible gravitational waves from massive torus

A massive torus surrounding a black hole may be unstable to the so-called Papaloizou-Pringle instability (PPI) [55]. The PPI sets in if the torus has particular angular momentum distribution. If the PPI occurs, the torus is deformed by non-axisymmetric perturbation and gravitational waves are emitted. Figure 22 displays the density and specific angular momentum distribution of the torus along the cylindrical coordinate on the equatorial plane for the N model with $\Gamma = 1.335$ and $T_{\text{rot}}/|W| \approx 0.009$. Immediately after the formation of the torus, the torus oscillates, and thus, we plot the profiles at $t - t_{\text{BH}} = 9000 t_g$, which is the time at which the oscillating perturbation of the torus is sufficiently damped. Here, j , $\bar{\rho}$, and R_g are the specific angular momentum, dimensionless density, and the gravitational radius of the black hole; $\bar{\rho}$ and R_g are defined by

$$\bar{\rho} \equiv \rho K^N c^{-2N}, \quad (5.15)$$

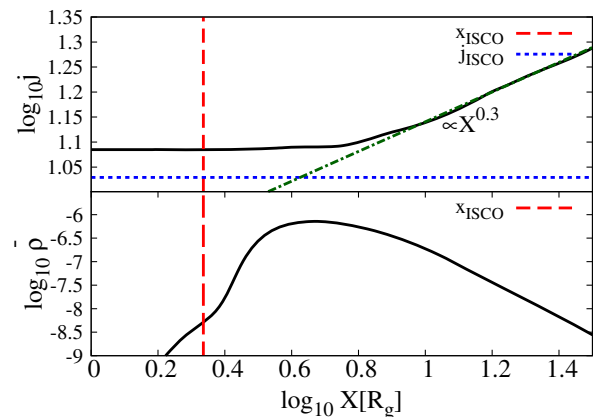


FIG. 22. The profiles of the specific angular momentum (upper panel) and dimensionless density (lower panel) distribution as functions of the radial coordinate on the equatorial plane at $t - t_{\text{BH}} = 9000 t_g$ for the N model with $\Gamma = 1.335$ and $T_{\text{rot}}/|W| \approx 0.009$. The red-dashed and blue-dotted curves denote the radius of the ISCO and the specific angular momentum which is needed for a test particle to rotate at the ISCO, respectively. The green dashed-dotted curve denotes a slope proportional to $X^{0.3}$.

$$R_g \equiv \frac{GM_{\text{BH}}}{c^2}, \quad (5.16)$$

respectively. Here K is the polytropic constant defined by Eq. (2.33). The peak of the density depends weakly on Γ and $T_{\text{rot}}/|W|$ and is located at $X \approx 5R_g$. For $X \lesssim 5R_g$, $j \approx \text{const}$, and for $X \gtrsim 5R_g$, $j \propto X^{0.3}$. The reason why $j \approx \text{const}$ at $X \lesssim X_{\text{ISCO}}$ is that a fraction of the torus material falls to the black hole from the inner edge of the torus due to the oscillation of the torus while conserving its specific angular momentum.

Previous general relativistic simulations show that the stability against the PPI depends on the profile of j and strength of the self-gravity of tori [56]. If a torus is strongly self-gravitating and has the specific angular momentum distribution of the form of $j \propto X^\beta$, the torus is unstable to the PPI if $\beta \lesssim 0.25$ [57]. The torus found in our present study is also self-gravitating and $\beta \approx 0$ at the density maximum, and hence, it may be unstable. To determine the stability to the PPI of these tori, we plan to perform a 3D numerical simulation in the future work.

Here, we estimate the frequency and amplitude of gravitational waves from the black hole-torus system assuming that the PPI hypothetically occurs. The amplitude of gravitational waves can be approximately estimated by using quadrupole formula as

$$h_{ij} \approx \frac{2G}{c^4 r_L} \ddot{Q}_{ij}, \quad (5.17)$$

where r_L and Q_{ij} are the luminosity distance and the mass quadrupole moment, respectively [58]. We assume that a fraction of the torus deforms into one clump and rotates with Keplerian motion around the black hole. We regard this system as a star with mass M_{clump} rotating around the central black hole with mass $M_{\text{BH}} (\gg M_{\text{clump}})$. Then, the frequency of gravitational waves measured by the observer, $f_{\text{gw}}^{(\text{obs})}$, can be approximated by

$$f_{\text{gw}}^{(\text{obs})} = \frac{1}{\pi(1+z)} \sqrt{\frac{GM_{\text{BH}}}{r_{\text{tor}}^3}}, \quad (5.18)$$

where z and r_{tor} are the cosmological redshift and the distance of the clump from the central black hole, respectively. In this system, the magnitude of \ddot{Q}_{ij} can be approximated by $M_{\text{clump}} v^2$, where v is the orbital velocity of the clump. Previous numerical simulation shows that if the PPI occurs, the system emits quasiperiodic gravitational waves and its emission will continue for $\gtrsim 100$ cycles if the viscosity of the torus is not very high [57]. Hence the peak amplitude of gravitational waves, h_{peak} , may be enhanced by approximately $\sqrt{100} = 10$ times. Then if the collapse of a SMS takes place $z = 5$, we get the typical peak frequency and amplitude of gravitational waves

$$f_{\text{gw}}^{(\text{obs})} \sim 1 \times 10^{-2} \left(\frac{z+1}{6}\right)^{-1} \left(\frac{r_{\text{tor}}}{5R_g}\right)^{-\frac{3}{2}} \left(\frac{M_{\text{BH}}}{10^5 M_\odot}\right)^{-1} \text{ Hz}, \quad (5.19)$$

$$h_{\text{peak}} \sim 2 \times 10^{-21} \left(\frac{M_{\text{tor}}}{0.05 M_{\text{BH}}}\right) \left(\frac{M_{\text{clump}}}{0.1 M_{\text{tor}}}\right) \left(\frac{M_{\text{BH}}}{10^5 M_\odot}\right) \times \left(\frac{r_{\text{tor}}}{5R_g}\right)^{-1} \left(\frac{r_L}{50 \text{ Gpc}}\right)^{-1} \left(\frac{N_{\text{cycle}}}{100}\right)^{\frac{1}{2}}. \quad (5.20)$$

Here, M_{tor} and N_{cycle} are the mass of the torus and the number of the cycles of gravitational waves, respectively. From Eqs. (5.19) and (5.20), we find that the typical frequency and amplitude of gravitational waves are $\approx 10^{-2}$ Hz and $\approx 10^{-21}$. These values correspond to the sensitive observation band of LISA [32] if the collapse of a SMS takes place at $z \lesssim 5$.

VI. CONCLUSION

We explored the gravitational collapse of rotating SMS cores employing realistic initial conditions and including the effects of nuclear burning. We showed that though the efficiency of nuclear burning exponentially grows just before the black-hole formation, its effect is negligible in our models. After the collapse, a fraction of the initial mass forms a torus surrounding the remnant black hole and drives an outflow. We also find that nuclear burning gives only a minor effect for the evolution of the torus.

We also studied the gravitational collapse of SMS cores with various adiabatic constants and rotation parameters turning off nuclear burning and analyzed quantitatively the mass of the torus, black-hole spin, and the property of the outflow. We found that the black-hole spin agrees well with our previous analytical predictions [30]. On the other hand, the mass of the torus is slightly smaller than the predicted value. This is because in our prediction, we regard each fluid element of the SMS core as a test particle, and assume that it has a circular orbit around the hypothetically formed black hole. However, in reality, each fluid element of the SMS core feels the pressure force, and falls in an elliptical orbit to the central black hole, and hence, a fraction of the fluid element falls into the black hole even though they have specific angular momentum larger than the value of ISCO.

If a SMS core is sufficiently rapidly rotating ($T_{\text{rot}}/|W| > 0.004$), the outflow would have mass $\approx 1\%$ of initial mass and kinetic energy 10^{54-56} erg with its velocity $\approx 0.2c$. The outflow would collide with the envelope of the SMS and forms shocks. We estimated the luminosity when the shocks reach the surface of the SMS and found that its typical luminosity and time scale are of order 10^{45} erg/s and 10 yrs, respectively. Exploring more detailed time evolution of the outflow and possibility for observing it is our future work. We note that a recent 3D

magnetohydrodynamic simulation suggests that the magnetic fields could enhance the amount of the outflow [59].

When the black hole forms, burst gravitational waves are emitted [31]. We found that the gravitational waveforms are characterized primarily by the ringdown oscillation associated with the quasinormal mode of the formed black holes. We also found that the amplitude of gravitational waves depends weakly on the values of $T_{\text{rot}}/|W|$ as long as it is of order 10^{-3} and the total radiated energy is $O(10^{-6})M_0c^2$. If the value of $T_{\text{rot}}/|W|$ is of $O(10^{-3})$, gravitational waves can be detected by LISA if the collapse of a SMS takes place at $z \lesssim 3$.

We also estimated the frequency and amplitude of gravitational waves assuming that the torus surrounding the central black hole may be deformed by the PPI. We found that if the PPI occurs, gravitational waves emitted from the torus may be observed by LISA [32] if the collapse of a SMS takes place at $z \lesssim 5$.

ACKNOWLEDGMENTS

We are grateful to Koh Takahashi whose comments and suggestions about nuclear burning were of inestimable value for our study. We also owe a very important debt to Kenta Kiuchi who gave us invaluable comments about numerical calculation. We also thank Yudai Suwa and Tatsuya Matsumoto for a helpful discussion. Numerical computations were performed on the supercomputer XC30 at CfCA of NAOJ, and XC40 at YITP of Kyoto University. This work was supported by Grant-in-Aid for Scientific Research (Grant Nos. 16H02183, 16K17706, 16H05341, 15H00782) of Japanese MEXT/JSPS.

APPENDIX A: CALCULATION OF THE NUCLEAR BURNING

The effect of nuclear burning might be able to be taken into account by naively adding nuclear energy generation rates as a source term of the evolution equation of the fluid with fixed chemical composition as [37]

$$\nabla_{\mu} T^{\mu\nu} = \frac{\rho_0 \dot{q} u^{\nu}}{c}, \quad (\text{A1})$$

$$\dot{q} = \dot{q}_{\text{CNO}} + \dot{q}_{3\alpha}. \quad (\text{A2})$$

However, we find that this method is not very appropriate to calculate the effects of nuclear burning even if the change of the chemical composition is negligible when we set the initial metallicity of order 10^{-3} .

To illustrate this fact, we compare the results of two simulations with the same initial conditions but with different formalisms to incorporate the effects of nuclear burning. One is the formalism described in Eq. (A1) (model T1), and the other is that described in Sec. II D (model T2). We set the initial condition which mimics model R1.d of

Ref. [37], that is, the SMS core is rotating at mass-shedding limit, its mass is $\approx 5 \times 10^5 M_{\odot}$, and its chemical composition is $(Y_p, X_{\alpha}, Z_C) = (0.748, 0.250, 0.002)$. We performed another simulation with the same condition as model T2 except initial metallicity chosen as $(Y_p, X_{\alpha}, Z_C) = (0.74, 0.25, 0.01)$ (model T3). We also performed simulations with the same initial conditions as models A1 and A3 (see Sec. III) with the formalism described in Eq. (A1) (models TA1 and TA3).

We find that for models TA1 and TA3, our results are essentially the same as those for models A1 and A3, respectively. Thus, we conclude that when we set the initial metallicity of order 10^{-9} , the differences between our formalism and formalism described in Eq. (A1) are negligible.

However, when we set the initial metallicity of order 10^{-3} , a considerable problem occurs. Figure 23 shows the time evolution of the ratio of the released rest-mass energy due to nuclear burning, Q , to the initial total energy, E_{ini} . Here, Q and E_{ini} are defined by

$$Q(t) \equiv \begin{cases} \int_0^t dt \int_V \rho_{0*} \dot{q} dV & (\text{T1}), \\ \text{Eq. (3.13)} & (\text{T2 and T3}), \end{cases} \quad (\text{A3})$$

and

$$E_{\text{ini}} \equiv (T_{\text{tot}} + U + W)(t = 0 \text{ s}), \quad (\text{A4})$$

respectively. The filled circle denotes the time ($t \approx 25000$ s) at which the system becomes unbound and starts exploding for model T1. We check that in the absence of the nuclear burning, this model does not explode. Thus this explosion is due to the nuclear burning. However, the value of Q is by more than one order of magnitude smaller

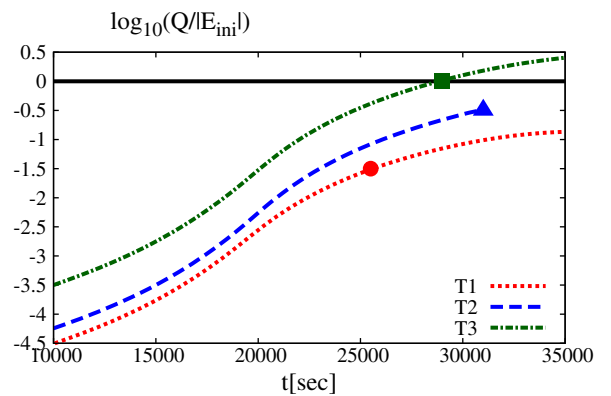


FIG. 23. Time evolution of the ratio of the released rest-mass energy due to nuclear burning to the initial total energy. The dotted, dashed, and dashed-dotted curves denote for models T1, T2, and T3, respectively. For models T1 and T3, the explosion is found at $t \approx 25000$ s (filled circle) and $t \approx 29000$ s (filled square), while for model T2, a black hole is formed at $t \approx 31000$ s (filled triangle), respectively.

than the value of $|E_{\text{ini}}|$ at this time. Thus, in terms of energy conservation, it is incomprehensible that the nuclear burning causes the explosion. Indeed, we find that for model T2, the nuclear burning cannot halt the collapse and the black hole is formed at $t \approx 31000$ s (filled triangle). We check that the chemical composition at the center of the SMS core for model T2 does not change approximately until $t \approx 25000$ s. Thus this difference would be due to the fact that Eq. (A1) violates the energy-momentum conservation. We suspect that even though the violation is much smaller than the total energy, this violation is accumulated and finally induces the unnatural increase of the total energy.

We also find that for model T3, the SMS core starts exploding at $t \approx 29000$ s (filled square). At this time, $Q \approx |E_{\text{ini}}|$ is realized, and thus, this explosion would be indeed due to the nuclear burning. We conclude that for the computation of the gravitational collapse of a SMS core, it is important to employ the formalism in which the conservation of the total energy is satisfied with the required level.

APPENDIX B: DEFINITION OF THE MASS AND ENERGY FLUX OF THE OUTFLOW

In this section, we define the mass and energy fluxes of the outflow by using the conservation of the total mass and energy. The local conservation equation for the energy-momentum tensor together with the Killing equation for a timelike Killing vector field ξ^μ gives

$$\nabla_\mu (T^\mu_{\nu} \xi^\nu) = 0. \quad (\text{B1})$$

For the analysis of the outflow, we assume that the space-time becomes a stationary state after the collapse. Then $(\partial_t)^\mu$ should be a timelike Killing vector field, and hence,

$$\nabla_\mu T^\mu_t = 0, \quad (\text{B2})$$

is realized. On the other hand, if we neglect nuclear burning after the collapse, the rest-mass density should be conserved, i.e.,

$$\nabla_\mu (\rho_0 u^\mu) = 0. \quad (\text{B3})$$

By using Eqs. (B2) and (B3), we get two equations of continuity as

$$\frac{\partial \rho_A}{\partial t} + \nabla \cdot \mathbf{f}_A = 0 (A = M, E), \quad (\text{B4})$$

where

$$\rho_M \equiv \rho_{0*}, \quad (\text{B5})$$

$$\rho_E \equiv -\rho_{0*} c^2 \left(\frac{h_0 u_t}{c^3} + \frac{P}{\rho_0 c^3 u^t} + 1 \right), \quad (\text{B6})$$

and

$$\mathbf{f}_M \equiv \rho_{0*} \mathbf{v}, \quad (\text{B7})$$

$$\mathbf{f}_E \equiv -\rho_{0*} c^2 \mathbf{v} \left(\frac{h_0 u_t}{c^3} + 1 \right). \quad (\text{B8})$$

Here, $\rho_{0*} \equiv \rho_0 \sqrt{-g} c u^t$ and h_0 are the weighted rest-mass density and the specific enthalpy, respectively. ρ_E is defined as the total energy density minus rest-mass energy density. Subscripts ‘‘M’’ and ‘‘E’’ denote the total mass and energy, respectively.

Assuming that the internal energy is much smaller than the kinetic and potential energy of the outflow, we define the fluid component which satisfies $u_t < -1$ as the outflow component. In the Newtonian approximation, u_t is written by

$$u_t \approx -1 + \frac{GM_{\text{BH}}}{R} - \frac{1}{2} v^2, \quad (\text{B9})$$

where M_{BH} , R , and v are the mass of the black hole, distance from the black hole, and velocity of the fluid element, respectively. Hence $u_t < -1$ is equivalent to $v^2/2 > GM_{\text{BH}}/R$ which implies that the fluid element is unbound.

To analyze the mass and energy of the outflow, we replace ρ_0 with ρ_0^{ejc} where ρ_0^{ejc} is defined by

$$\rho_0^{\text{ejc}} \equiv \rho_0 \Theta(-u_t - 1), \quad (\text{B10})$$

$$\Theta(x) \equiv \begin{cases} 1 & x \geq 0, \\ 0 & x < 0. \end{cases} \quad (\text{B11})$$

We denote the quantities associated with the unbound material by subscript ‘‘ejc’’.

Then, the mass and energy of the outflow, which are ejected from the domain $\sqrt{X^2 + Z^2} < D$, can be written as

$$\begin{aligned} A_{\text{ejc}}(D, t) &= - \int_0^t dt' \int \mathbf{f}_A^{\text{ejc}} \cdot d\mathbf{S} \\ &= \int_0^t dt' \int_0^{\frac{\pi}{2}} d\theta (-4\pi D^2 \mathbf{f}_A^{\text{ejc}} \cdot \hat{\mathbf{r}} \sin \theta) (A = M, E), \end{aligned} \quad (\text{B12})$$

where $\hat{\mathbf{r}}$ and θ are the radial unit vector and the polar angle, i.e., $\tan \theta = X/Z$. We define the total mass and energy of the outflow by

$$A_{\text{ejc}}(D) \equiv A_{\text{ejc}}(D, t = t^*), \quad (\text{B13})$$

where t^* is the time at which all of the unbound fluid elements finish escaping from the domain $\sqrt{X^2 + Z^2} < D$.

The total mass and energy of the outflow also can be defined by

$$A_{\text{oflw}}(t) \equiv \int_{V'} \rho_A^{\text{ejc}} dV (A = M, E). \quad (\text{B14})$$

$A_{\text{oflw}}(t = \infty)$ should correspond to $A_{\text{ejc}}(D)$ irrespective of the value of D if the total mass and energy of the outflow are conserved. Finally, we define the total kinetic energy, T_{oflw} , the radial component of the total kinetic energy, T_{oflw}^r , the total internal energy, U_{oflw} , and the total gravitational potential energy, W_{oflw} , of the outflow by

$$T_{\text{oflw}}(t) \equiv \int_{V'} \frac{1}{2} \rho_{0*}^{\text{ejc}} c^2 (1 - (\alpha c u^t)^2) dV, \quad (\text{B15})$$

$$T_{\text{oflw}}^r(t) \equiv \int_{V'} \frac{1}{2c} \rho_{0*}^{\text{ejc}} h_0 v^r u_r dV, \quad (\text{B16})$$

$$U_{\text{oflw}}(t) \equiv \int_{V'} \rho_*^{\text{ejc}} \epsilon dV, \quad (\text{B17})$$

and

$$W_{\text{oflw}}(t) \equiv E_{\text{oflw}} - T_{\text{oflw}} - U_{\text{oflw}}, \quad (\text{B18})$$

respectively. Here, $\rho_*^{\text{ejc}} \equiv \rho \sqrt{-g} c u^t \Theta(-u_t - 1)$.

APPENDIX C: INITIAL PERTURBATION DEPENDENCE OF THE OUTFLOW

In this section, we analyze the dependence of total mass and energy of the outflow on D_T . In this analysis, we performed additional simulations with $T_{\text{rot}}/|W| = 0.005$ for the helium-burning models (model A5).

Figures 24 and 25 display the dependence of the total mass and energy of the outflow on D_T for the helium-burning models with three rotation parameters, i.e., $T_{\text{rot}}/|W| = 0.002$ (model A2), 0.005 (model A5), and ≈ 0.009 (model A4) at $t - t_{\text{BH}} = 5000 t_g$, respectively. Here, M_{oflw} and E_{oflw} are defined by Eq. (B14). The total mass and energy of the outflow increase approximately linearly with D_T . Thus we can estimate the total mass and energy of the outflow of $D_T = 0$ by using linear fitting formula. Each of three lines of Figs. 24 and 25 denote the linear fitting function for each value of $T_{\text{rot}}/|W|$. Here the value with $D_T = 0$ should be regarded as the physical value.

We find that for $T_{\text{rot}}/|W| = 0.002$ (model A2), 0.005 (model A5), and ≈ 0.009 (model A4), the value of M_{oflw} is

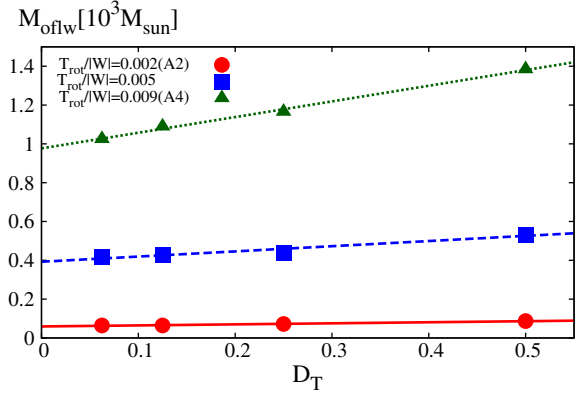


FIG. 24. The total mass of the outflow, M_{oflw} , as a function of D_T with $T_{\text{rot}}/|W| = 0.002$ (model A2, filled-circles), 0.005 (model A5, filled-squares), and 0.009 (model A4, filled-triangles) at $t - t_{\text{BH}} = 5000 t_g$ for the helium-burning models. The solid, dashed, and dotted curves denote the linear fitting function for the value of $T_{\text{rot}}/|W| = 0.002$, 0.005 , and 0.009 , respectively.

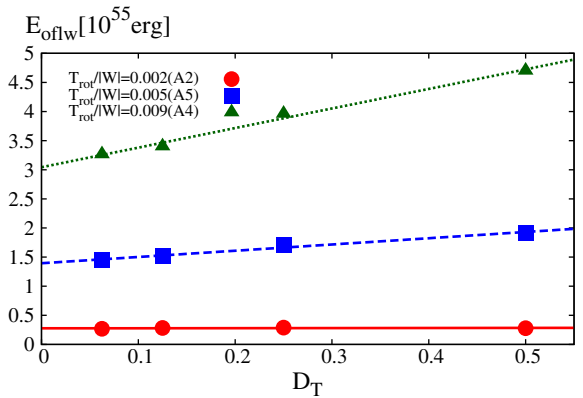


FIG. 25. The total energy of the outflow, E_{oflw} , as a function of D_T with $T_{\text{rot}}/|W| = 0.002$ (model A2, filled-circles), 0.005 (model A5, filled-squares), and 0.009 (model A4, filled-triangles) at $t - t_{\text{BH}} = 5000 t_g$ for the helium-burning models. The solid, dashed, and dotted curves denote the linear fitting function for the value of $T_{\text{rot}}/|W| = 0.002$, 0.005 , and 0.009 , respectively.

overestimated with $D_T = 0.5$ by 47%, 35%, and 42%, and E_{oflw} is overestimated by 1%, 37%, and 54%, respectively.

We speculate the reason why M_{oflw} and E_{oflw} are increasing functions of D_T is as follows: For the larger value of D_T , the fluid falls with larger velocity, and hence, shock heating more efficiently occurs around the inner edge of the torus, and the bubble which we describe in Sec. IV A is more strongly pushed by the torus.

- [1] V. Bromm and A. Loeb, *Astrophys. J.* **596**, 34 (2003).
- [2] D. Sobral, J. Matthee, B. Darvish, D. Schaerer, B. Mobasher, H. J. A. Röttgering, S. Santos, and S. Hemmati, *Astrophys. J.* **808**, 139 (2015).
- [3] B. Agarwal, J. L. Johnson, E. Zackrisson, I. Labbe, F. C. van den Bosch, P. Natarajan, and S. Khochfar, *Mon. Not. R. Astron. Soc.* **460**, 4003 (2016).
- [4] K. Inayoshi, K. Omukai, and E. Tasker, *Mon. Not. R. Astron. Soc.* **445**, L109 (2014).
- [5] B. L. Davis, J. C. Berrier, L. Johns, D. W. Shields, M. T. Hartley, D. Kenefick, J. Kenefick, M. S. Seigar, and C. H. S. Lacy, *Astrophys. J.* **789**, 124 (2014).
- [6] S. Hirano, T. Hosokawa, N. Yoshida, K. Omukai, and H. W. Yorke, *Mon. Not. R. Astron. Soc.* **448**, 568 (2015).
- [7] X.-B. Wu *et al.*, *Nature (London)* **518**, 512 (2015).
- [8] D. J. Mortlock *et al.*, *Nature (London)* **474**, 616 (2011).
- [9] M. Volonteri and M. J. Rees, *Astrophys. J.* **633**, 624 (2005).
- [10] P. Madau, F. Haardt, and M. Dotti, *Astrophys. J. Lett.* **784**, L38 (2014).
- [11] K. Inayoshi, Z. Haiman, and J. P. Ostriker, *Mon. Not. R. Astron. Soc.* **459**, 3738 (2016).
- [12] T. Hosokawa, H. W. Yorke, K. Inayoshi, K. Omukai, and N. Yoshida, *Astrophys. J.* **778**, 178 (2013).
- [13] H. Umeda, T. Hosokawa, K. Omukai, and N. Yoshida, *Astrophys. J. Lett.* **830**, L34 (2016).
- [14] L. Haemmerlé, T. E. Woods, R. S. Klessen, A. Heger, and D. J. Whalen, *arXiv:1705.09301*.
- [15] T. E. Woods, A. Heger, D. J. Whalen, L. Haemmerlé, and R. S. Klessen, *Astrophys. J. Lett.* **842**, L6 (2017).
- [16] J. R. Bond, W. D. Arnett, and B. J. Carr, *Astrophys. J.* **280**, 825 (1984).
- [17] K. Omukai, *Astrophys. J.* **546**, 635 (2001).
- [18] S. Chon, S. Hirano, T. Hosokawa, and N. Yoshida, *Astrophys. J.* **832**, 134 (2016).
- [19] J. A. Regan *et al.*, *Nature Astronomy* **1**, 0075 (2017).
- [20] K. Inayoshi and K. Omukai, *Mon. Not. R. Astron. Soc.* **422**, 2539 (2012).
- [21] A. Loeb and F. A. Rasio, *Astrophys. J.* **432**, 52 (1994).
- [22] M. A. Latif, D. R. G. Schleicher, W. Schmidt, and J. Niemeyer, *Mon. Not. R. Astron. Soc.* **430**, 588 (2013).
- [23] J. A. Regan, P. H. Johansson, and M. G. Haehnelt, *Mon. Not. R. Astron. Soc.* **439**, 1160 (2014).
- [24] F. Becerra, T. H. Greif, V. Springel, and L. E. Hernquist, *Mon. Not. R. Astron. Soc.* **446**, 2380 (2015).
- [25] S. Chandrasekhar, *Astrophys. J.* **140**, 417 (1964).
- [26] P. Ledoux, *Astrophys. J.* **102**, 143 (1945).
- [27] W. A. Fowler, *Astrophys. J.* **144**, 180 (1966).
- [28] J.-L. Tassoul, *Theory of rotating stars* (Princeton University Press, Princeton, NJ, USA, 1978).
- [29] T. W. Baumgarte and S. L. Shapiro, *Astrophys. J.* **526**, 941 (1999).
- [30] M. Shibata, H. Uchida, and Y. Sekiguchi, *Astrophys. J.* **818**, 157 (2016).
- [31] M. Shibata, Y. Sekiguchi, H. Uchida, and H. Umeda, *Phys. Rev. D* **94**, 021501(R) (2016).
- [32] H. Audley *et al.*, *arXiv:1702.00786*.
- [33] C. Reisswig, C. D. Ott, E. Abdikamalov, R. Haas, P. Mösta, and E. Schnetter, *Phys. Rev. Lett.* **111**, 151101 (2013).
- [34] T. Matsumoto, D. Nakauchi, K. Ioka, A. Heger, and T. Nakamura, *Astrophys. J.* **810**, 64 (2015).
- [35] T. Matsumoto, D. Nakauchi, K. Ioka, and T. Nakamura, *Astrophys. J.* **823**, 83 (2016).
- [36] G. M. Fuller, S. E. Woosley, and T. A. Weaver, *Astrophys. J.* **307**, 675 (1986).
- [37] P. J. Montero, H.-T. Janka, and E. Müller, *Astrophys. J.* **749**, 37 (2012).
- [38] K.-J. Chen, A. Heger, S. Woosley, A. Almgren, D. J. Whalen, and J. L. Johnson, *Astrophys. J.* **790**, 162 (2014).
- [39] Y. T. Liu, S. L. Shapiro, and B. C. Stephens, *Phys. Rev. D* **76**, 084017 (2007).
- [40] M. Shibata and T. Nakamura, *Phys. Rev. D* **52**, 5428 (1995).
- [41] T. W. Baumgarte and S. L. Shapiro, *Phys. Rev. D* **59**, 024007 (1998).
- [42] M. Campanelli, C. O. Lousto, P. Marronetti, and Y. Zlochower, *Phys. Rev. Lett.* **96**, 111101 (2006).
- [43] J. G. Baker, J. Centrella, D.-I. Choi, M. Koppitz, and J. van Meter, *Phys. Rev. Lett.* **96**, 111102 (2006).
- [44] M. Shibata, *Numerical Relativity* (World Scientific Publishing Co, Singapore, 2016).
- [45] M. Shibata and Y.-i. Sekiguchi, *Phys. Rev. D* **71**, 024014 (2005).
- [46] M. Alcubierre, B. Brügmann, D. Holz, R. Takahashi, S. Brandt, E. Seidel, and J. Thornburg, *Int. J. Mod. Phys. D* **10**, 273 (2001).
- [47] M. Shibata, *Phys. Rev. D* **67**, 024033 (2003).
- [48] K. Takahashi, T. Yoshida, H. Umeda, K. Sumiyoshi, and S. Yamada, *Mon. Not. R. Astron. Soc.* **456**, 1320 (2016).
- [49] N. Itoh, H. Hayashi, A. Nishikawa, and Y. Kohyama, *Astrophys. J. Suppl. Ser.* **102**, 411 (1996).
- [50] G. B. Cook, S. L. Shapiro, and S. A. Teukolsky, *Astrophys. J.* **398**, 203 (1992).
- [51] Y. B. Zeldovich and I. D. Novikov, *Relativistic astrophysics. Vol. 1: Stars and relativity* (University of Chicago Press, Chicago, USA, 1971).
- [52] N. I. Shakura and R. A. Sunyaev, *Astron. Astrophys.* **24**, 337 (1973)..
- [53] J. M. Bardeen, W. H. Press, and S. A. Teukolsky, *Astrophys. J.* **178**, 347 (1972).
- [54] W. H. Lee and E. Ramirez-Ruiz, *Astrophys. J.* **641**, 961 (2006).
- [55] J. C. B. Papaloizou and J. E. Pringle, *Mon. Not. R. Astron. Soc.* **208**, 721 (1984).
- [56] O. Korobkin, E. B. Abdikamalov, E. Schnetter, N. Stergioulas, and B. Zink, *Phys. Rev. D* **83**, 043007 (2011).
- [57] K. Kiuchi, M. Shibata, P. J. Montero, and J. A. Font, *Phys. Rev. Lett.* **106**, 251102 (2011).
- [58] C. W. Misner, K. S. Thorne, and J. A. Wheeler, *Gravitation* (W.H. Freeman and Co., San Francisco, USA, 1973).
- [59] L. Sun, V. Paschalidis, M. Ruiz, and S. L. Shapiro, *Phys. Rev. D* **96**, 043006 (2017).